Molecular Cell

Article

hRpn13 shapes the proteome and transcriptome through epigenetic factors HDAC8, PADI4, and transcription factor NF-κB p50

Graphical abstract

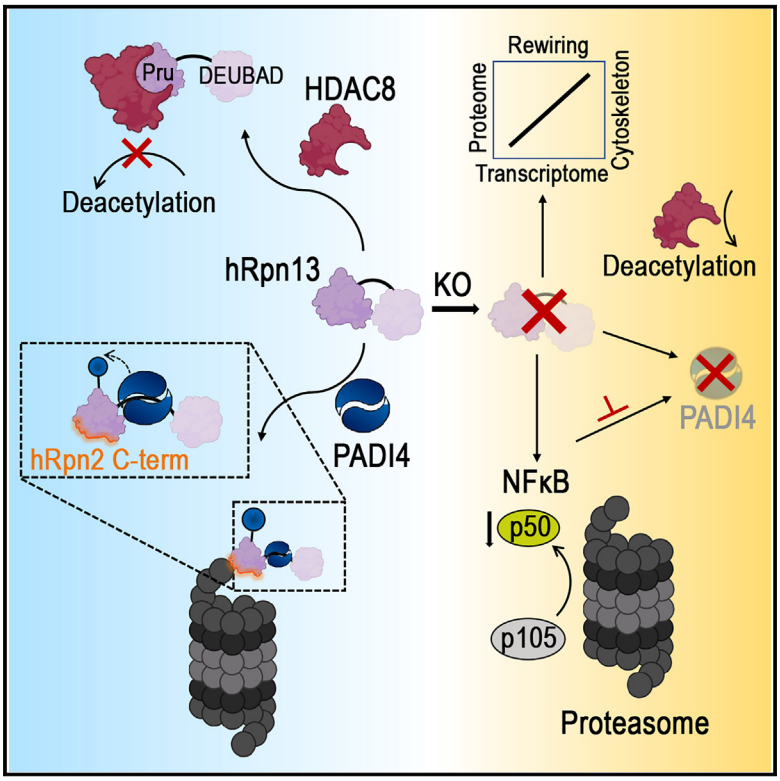

Highlights

- hRpn13 loss alters expression of cytoskeletal, epigenetic, and immune response factors
- PADI4 binds and citrullinates hRpn13, which, when off proteasomes, can also bind HDAC8
- PADI4 binds, citrullinates, and affects the peptidase activity of proteasomes
- hRpn13 loss reduces NF-κB p50, the inhibition of which reduces PADI4 and HDAC8

Authors

Vasty Osei-Amponsa, Monika Chandravanshi, Xiuxiu Lu, ..., Michelle E. Clapp, Raj Chari, Kylie J. Walters

Correspondence

kylie.walters@nih.gov

In brief

Osei-Amponsa et al. discover hRpn13 interaction with epigenetic factors physically and functionally both on and off proteasomes and contribution to NF-κB p50 production. These and additionally identified hRpn13 transcriptional requirements provide insights into its cellular impact beyond its known role at proteasomes and rationale for anti-cancer activities of hRpn13 PROTACs.

Osei-Amponsa et al., 2024, Molecular Cell *84*, 522–537
February 1, 2024
https://doi.org/10.1016/j.molcel.2023.11.035

CellPress

CellPress

Molecular Cell

Article

hRpn13 shapes the proteome and transcriptome through epigenetic factors HDAC8, PADI4, and transcription factor NF-κB p50

Vasty Osei-Amponsa,[1] Monika Chandravanshi,[1] Xiuxiu Lu,[1] Valentin Magidson,[2] Sudipto Das,[3] Thorkell Andresson,[3] Marzena Dyba,[4] Venkata R. Sabbasani,[5] Rolf E. Swenson,[5] Caroline Fromont,[6] Biraj Shrestha,[7] Yongmei Zhao,[7] Michelle E. Clapp,[8] Raj Chari,[8] and Kylie J. Walters[1,9,*]

[1]Protein Processing Section, Center for Structural Biology, Center for Cancer Research, National Cancer Institute, National Institutes of Health, Frederick, MD 21702, USA

[2]Optical Microscopy and Image Analysis Laboratory, Center for Cancer Research, National Cancer Institute, National Institutes of Health, Frederick, MD 21702, USA

[3]Protein Characterization Laboratory, Cancer Research Technology Program, Frederick National Laboratory for Cancer Research, Leidos Biomedical Research, Inc, Frederick, MD 21702, USA

[4]Biophysics Resource, Center for Structural Biology, National Cancer Institute, National Institutes of Health, Frederick, MD 21702, USA

[5]Chemistry and Synthesis Center, National Heart, Lung, and Blood Institute, National Institutes of Health, Bethesda, MD 20892, USA

[6]Sequencing Facility, Cancer Research and Technology Program, Frederick National Laboratory for Cancer Research, Frederick, MD 21701, USA

[7]Sequencing Facility Bioinformatics Group, Biomedical Informatics and Data Science Directorate, Frederick National Laboratory for Cancer Research, Frederick, MD 21701, USA

[8]Genome Modification Core, Frederick National Laboratory for Cancer Research, Frederick, MD 21702, USA

[9]Lead contact

*Correspondence: kylie.walters@nih.gov

https://doi.org/10.1016/j.molcel.2023.11.035

SUMMARY

The anti-cancer target hRpn13 is a proteasome substrate receptor. However, hRpn13-targeting molecules do not impair its interaction with proteasomes or ubiquitin, suggesting other critical cellular activities. We find that hRpn13 depletion causes correlated proteomic and transcriptomic changes, with pronounced effects in myeloma cells for cytoskeletal and immune response proteins and bone-marrow-specific arginine deiminase PADI4. Moreover, a PROTAC against hRpn13 co-depletes PADI4, histone deacetylase HDAC8, and DNA methyltransferase MGMT. PADI4 binds and citrullinates hRpn13 and proteasomes, and proteasomes from PADI4-inhibited myeloma cells exhibit reduced peptidase activity. When off proteasomes, hRpn13 can bind HDAC8, and this interaction inhibits HDAC8 activity. Further linking hRpn13 to transcription, its loss reduces nuclear factor κB (NF-κB) transcription factor p50, which proteasomes generate by cleaving its precursor protein. NF-κB inhibition depletes hRpn13 interactors PADI4 and HDAC8. Altogether, we find that hRpn13 acts dually in protein degradation and expression and that proteasome constituency and, in turn, regulation varies by cell type.

INTRODUCTION

Biological factors linked to specific processes are often studied in that context, which can mask other interactions with different machineries in distinct cellular compartments. hRpn13 is a target for myeloma therapy and is characterized functionally as a proteasomal component.[1] However, hRpn13 has also been suggested to have extra-proteasomal functions that remain little understood, and disrupting hRpn13 has profound effects on cell function. Growth of myeloma, acute leukemia, colorectal, gastric, and ovarian cancer cells is inhibited by hRpn13 loss.[2–9] An hRpn13-targeting peptomimetic reduces cell viability,[10] while bis-benzylidine compounds[11–13] and hRpn13 proteolysis-targeting chimera (PROTAC) XL5-VHL2[14] induces hRpn13-dependent apoptosis.[2,4,14,15]

hRpn13 has a pleckstrin-like receptor for ubiquitin (Pru) domain, which binds ubiquitin[16–18] and the extreme C terminus of proteasome subunit hRpn2,[15,19,20] and a deubiquitinase adaptor (DEUBAD) domain, which binds UCHL5/Uch37,[21–23] a deubiquitinase that hydrolyzes branched ubiquitin chains of mixed linkage (K48/K6, K48/K11, and K48/K63).[24] The two hRpn13 domains are separated by >100 intrinsically disordered amino acids and bind each other—an interaction that lowers Pru affinity for ubiquitin when hRpn13 is off proteasomes.[25] In myeloma cells, the proteasome cleaves hRpn13 to generate an $hRpn13^{Pru}$ fragment with an intact Pru and no DEUBAD,[14]

thereby decoupling UCHL5 activity from hRpn13 and proteasomes.[14] The proteasome also partially cleaves the nuclear factor κB (NF-κB) p105 precursor protein to generate transcriptionally active p50,[26] linking proteasome activity to gene expression through the NF-κB pathway,[26] which controls transcription in response to infection and cell stress.

The mechanism of hRpn13-dependent apoptosis remains unclear, as hRpn13-targeting molecules that induce apoptosis do not impair its interaction with proteasomes or ubiquitin.[11,14] To study further the importance of hRpn13 and its potential as an anti-cancer target, we examined the impact of losing hRpn13 or its Pru in colon cancer and myeloma cells. We find that hRpn13 loss causes widespread changes to both the proteome and transcriptome and uncover a functional network that links hRpn13 to proteins that regulate gene expression.

RESULTS

hRpn13 loss from myeloma cells rewires cytoskeletal and immune response proteins

Because multiple myeloma responds to proteasome inhibition, we measured proteomic changes caused by hRpn13 Pru deletion from myeloma cells. hRpn13 is encoded by the *ADRM1* gene, and we used *ADRM1*-edited RPMI 8226 cells (*trRpn13-MM2*), which express an N-terminally truncated protein at greatly reduced levels that begins from M109 (trRpn13; Figure S1A) and cannot bind the proteasome.[14] We subjected *trRpn13-MM2* or the parental *wild-type* (*WT*) cells to tandem mass tag-mass spectrometry (TMT-MS) and generated a volcano plot of the comparative protein abundance with p value. Pervasive changes in the proteome were detected following hRpn13 loss (Figures 1A and S1B), with consistency between technical replicates (Figure 1B). As expected, hRpn13 was the most reduced protein (Figure 1B).

Gene ontology (GO) analyses revealed affected proteins to contribute to the cytoskeleton, ubiquitin-proteasome system, immune response, metabolism, regulation, and transport (Figure 1C; Table S1). UCHL5 was reduced (Figures 1A, 1B, and S1B), consistent with previous studies of hRpn13 deletion or knockdown,[4,21,27] as was melanoma antigen family member C2 (MAGEC2), which activates the ubiquitin E3 ligase TRIM28[28] and the chromatin-modifying enzyme peptidyl arginine deiminase 4 (PADI4), which deiminates arginine (Figures 1A, 1B, and S1B). We also found O-6-methylguanine-DNA methyltransferase (MGMT) reduced (Figures 1A, 1B, and S1B), consistent with a report of hRpn13 regulation of MGMT in glioblastoma cells.[29]

We immunoprobed *WT* and *trRpn13-MM2* cell lysates for various proteins based on the TMT-MS results and antibody availability, with β-actin as a loading control. As expected,[14] *trRpn13-MM2* expressed trRpn13 at reduced levels (Figure 1D); the anti-hRpn13 antibodies used recognize the region spanning residues 100–200 (Figure S1A). Moreover, the previously described[14] hRpn13^{Pru} protein, which lacks DEUBAD, was detected in the parental cells with full-length hRpn13. We quantified the abundance of hRpn13^{Pru} relative to full-length hRpn13 in *WT* cells to find a 9-fold reduction and 5.4-fold reduction of trRpn13 relative to hRpn13^{Pru} (Figure S1C), indicating that relative to full-length hRpn13 in *WT* cells, trRpn13 in *trRpn13-MM2* cells is ~50-fold reduced. Validating the TMT-MS data, cytoskeletal protein myosin heavy chain 10 (MYH10) was enriched; UCHL5, PADI4, and MGMT were reduced; and HDAC8 was unaltered (Figure 1D).

Loss of hRpn13 Pru reduces PADI4 levels

To evaluate the contribution of the Pru domain specifically, we used another clonal cell line (*trRpn13-MM1*) that expresses higher levels of trRpn13 than *trRpn13-MM2* and also full-length hRpn13, albeit at barely detectable levels.[14] TMT-MS experiments yielded a volcano plot of comparative protein abundance with p value. As expected, hRpn13 was reduced and consistent with *trRpn13-MM2*, PADI4, myosin 1E (MYO1E), Bruton's tyrosine kinase (BTK), and actin-like 8 (ACTL8) were also reduced, whereas phosphodiesterase 5A (PDE5A), spartin (SPART), formin-like protein 2 (FMNL2), and β-tubulin 4A (TUBB4A) were increased compared with *WT* (Figures 2A and 2B). MGMT, actin-binding protein actinin alpha 1 (ACTN1), and MYH10 were not detected in this experiment. Immunoblotting indicated depletion of PADI4 in both *trRpn13-MM1* and *trRpn13-MM2* cells, whereas UCHL5 and MGMT were reduced in *trRpn13-MM1* compared with *WT*, but at higher levels than in *trRpn13-MM2*. MYH10 was detected only in *trRpn13-MM2* cells (Figure 2C).

We previously described HCT116-edited cell lines with deletion of hRpn13 (*ΔhRpn13*), UCHL5 (*ΔUCHL5*), or as with RPMI 8226 *trRpn13-MM1/2*, a truncated hRpn13 protein that begins at M109 (*trRpn13*).[4] We used these cell lines to decouple the impact of UCHL5 deletion from loss of hRpn13. Immunoprobing lysates from these cell lines confirmed expression of full-length hRpn13 in *WT* and *ΔUCHL5* cells, trRpn13 in *trRpn13* cells, and an absence of hRpn13 and UCHL5 in *ΔhRpn13* and *ΔUCHL5* cells, respectively (Figure 2D). Consistent with observations in *trRpn13-MM1* and *trRpn13-MM2* cells (Figure 2C), *trRpn13* and *ΔhRpn13* cells indicated WT and reduced levels of UCHL5 and MGMT, respectively (Figure 2D); HDAC8 abundance was not affected. MGMT was not reduced in *ΔUCHL5* cells (Figure 2D), indicating that its reduction in *ΔhRpn13* cells is not caused by reduced UCHL5 or loss of hRpn13 binding to the proteasome, as trRpn13 is unable to bind proteasomes.[4]

HCT116 cells are easier to transfect than RPMI 8226 cells. Using small interfering RNAs (siRNAs), we knocked down hRpn13 levels in HCT116 cells, immunoprobed for UCHL5 and MGMT, and found each reduced with HDAC8 unaffected (Figure 2E). Thus, an intact hRpn13 Pru is required for endogenous PADI4 levels but not for UCHL5 or MGMT. We next tested whether MGMT could be boosted in HCT116 cells by over-expression of hRpn13, to find both MGMT and hRpn13^{Pru} increased in FLAG-tagged hRpn13-expressing cells compared with an empty vector control (Figure 2F). We attempted to reintroduce hRpn13 into *trRpn13-MM1/2* by a lentiviral cDNA-based approach. Immunoprobing the lysates from *WT* or *trRpn13-MM1/2* cells, with and without transduction of *ADRM1* cDNA, indicated only low levels of hRpn13 expression (Figure 2G). Nonetheless, MYH10 was reduced in hRpn13-expressing *trRpn13-MM2* cells (Figure 2G); PADI4 and MGMT were not rescued following expression of hRpn13 in *trRpn13-MM1/2* cells. Altogether, these data indicate that hRpn13 reintroduced into *trRpn13-MM1/2* cells can repristinate MYH10, but not PADI4 or MGMT levels; however, MGMT levels are boosted in HCT116 cells by over-expressed hRpn13.

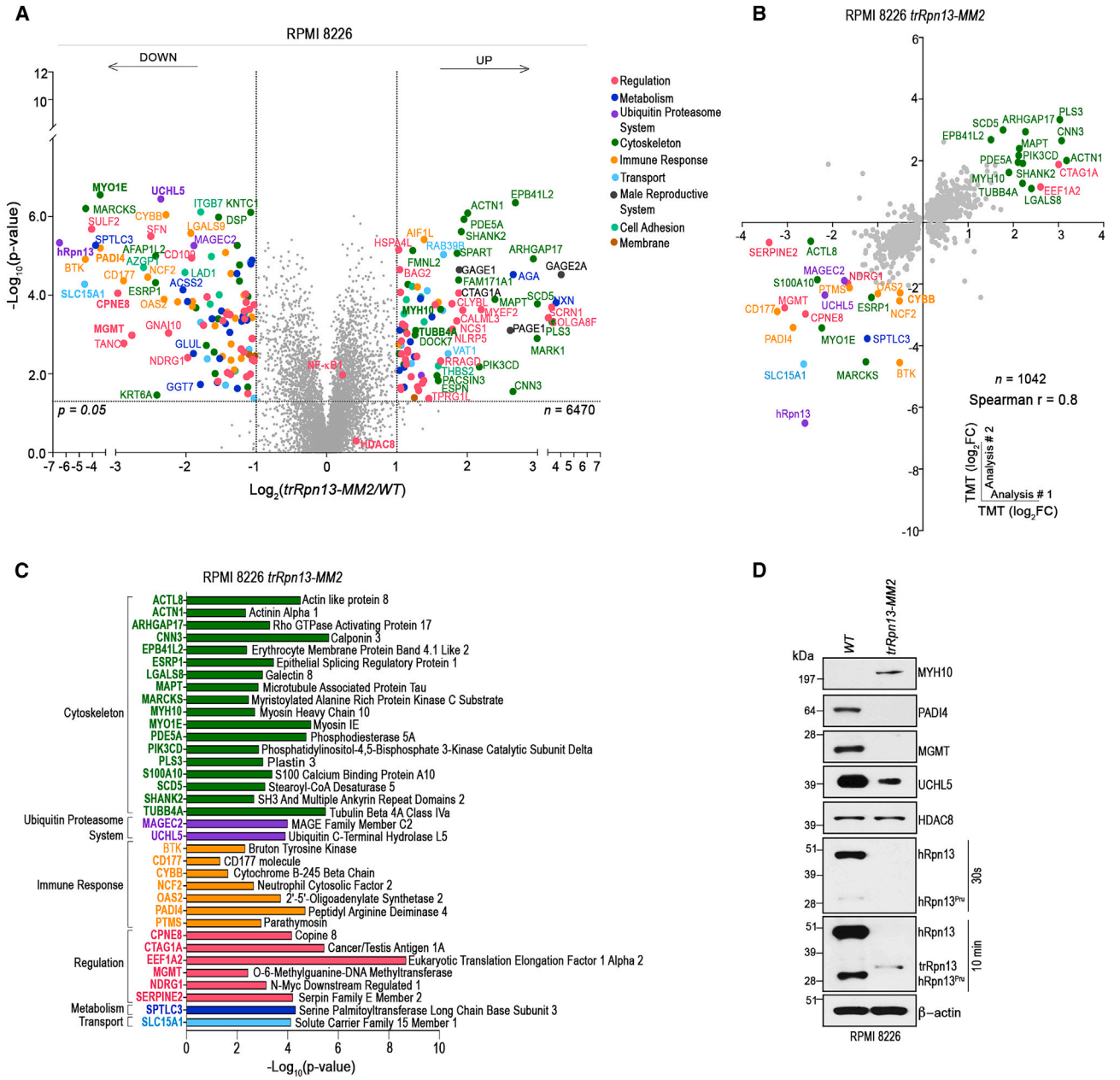

Figure 1. hRpn13 loss from myeloma cells reconfigures the cytoskeletal, immune response, and epigenetic proteome

(A) Volcano plot of fold change in protein abundance (x axis, log_2) with p value (y axis, $-log_{10}$) for *trRpn13-MM2* relative to *WT*. n, number of proteins analyzed.

(B) Plot of TMT-MS technical replicates from (A) (y axis) and Figure S1B (x axis) for data with p value < 0.05 and Spearman rank correlation included.

(C) Proteins significantly altered ($-log_{10}$ (p value) > 1.3) as shown in (B), analyzed by GO.

(D) Immunoblot of lysates from RPMI 8226 *WT* or *trRpn13-MM2* cells as indicated.

See also Figure S1.

Proteome alterations following hRpn13 loss correlate with transcriptomic changes

Myeloma cells are cancerous plasma cells with a specialized cytoskeleton and immune response. We were interested in how the cellular response to hRpn13-editing varies across cell lines and evaluated the proteomic data from hRpn13-edited HCT116 cells. As expected, significantly reduced hRpn13 levels were detected in *ΔhRpn13* (Figure S2A) and *trRpn13* (Figure S2B) cells. GO analysis revealed that cytoskeletal, regulatory, metabolic, and immune responses, as well as trafficking pathways, responded to hRpn13-editing (Figures S2A and S2B), consistent with *trRpn13-MM1/2* (Figures 1A and 2A), though the individually affected proteins varied. One-third of proteins significantly altered by hRpn13 loss in our myeloma datasets were absent

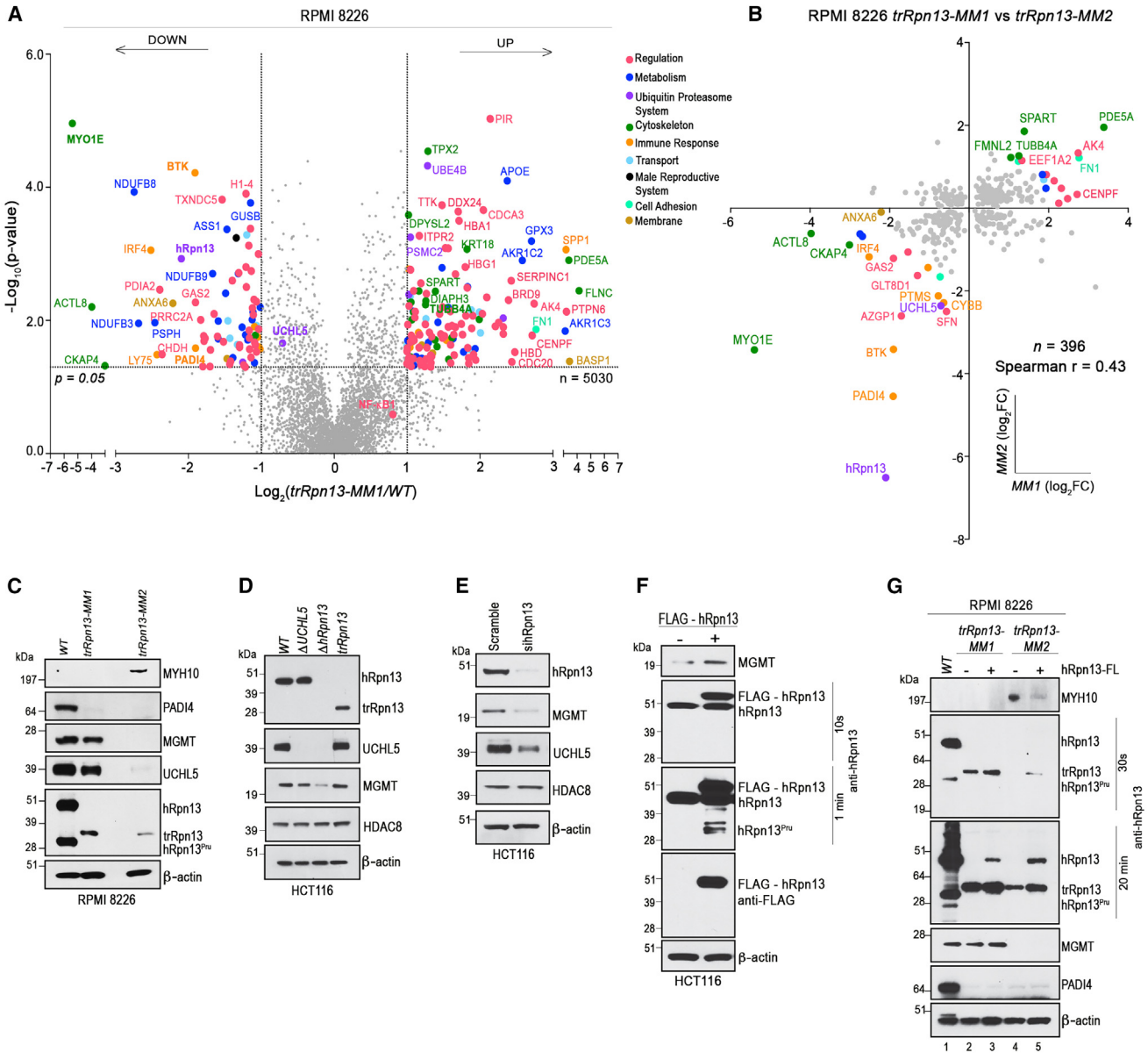

Figure 2. Deleting hRpn13 Pru depletes PADI4, with loss of full-length hRpn13 reducing MGMT and increasing MYH10

(A) Volcano plot of fold change in protein abundance (x axis, $\log_2$) and p value (y axis, $-\log_{10}$) for *trRpn13-MM1* relative to *WT*.

(B) Plot of change in protein abundance ($\log_2$) in *trRpn13-MM1* (x axis, A) versus *trRpn13-MM2* (y axis, Figure 1A) relative to *WT*.

(C) Immunoblots of lysates from RPMI 8226 *WT*, *trRpn13-MM1*, or *trRpn13-MM2* probed as indicated.

(D) Immunoblots of lysates from HCT116 *WT*, *ΔUCHL5*, *ΔhRpn13*, or *trRpn13* cells probed as indicated.

(E) Immunoblots of HCT116 *WT* cells treated for 48 h with a scrambled control or siRNA targeting hRpn13 (sihRpn13) probed as indicated.

(F) Lysates from HCT116 *WT* cells following 48-h transfection with FLAG-hRpn13 (+) or empty vector (−), immunoprobed as indicated.

(G) Immunoblots of lysates from RPMI 8226 *WT*, *trRpn13-MM1*, or *trRpn13-MM2* following lentiviral transduction of full-length hRpn13 (+) or untreated (−) immunoprobed as indicated. FL, full length.

from HCT116 cells, including PADI4, which is specific to bone marrow and spleen (https://www.ncbi.nlm.nih.gov/gene/23569#gene-expression). A previous study in HCT116 cells[30] found (similar to our study) UCHL5, calcium-binding protein S100A4, and other S100 proteins reduced following hRpn13 deletion (Figure S2A), but no other overlap was observed (Figure S2C). Immunoprobing for S100A14 validated reduction in *trRpn13* cells, whereas TACSTD2 varied (Figures S2A, S2B, and S2D).

The cytoskeleton-associated proteins upregulated in *trRpn13-MM2* were not affected in the HCT116-edited cells (Figure S3), and those that were affected varied between *ΔhRpn13* and *trRpn13* (Figures S2A versus S2B). As expected from the inherent differences between myeloma and colon cancer cells,

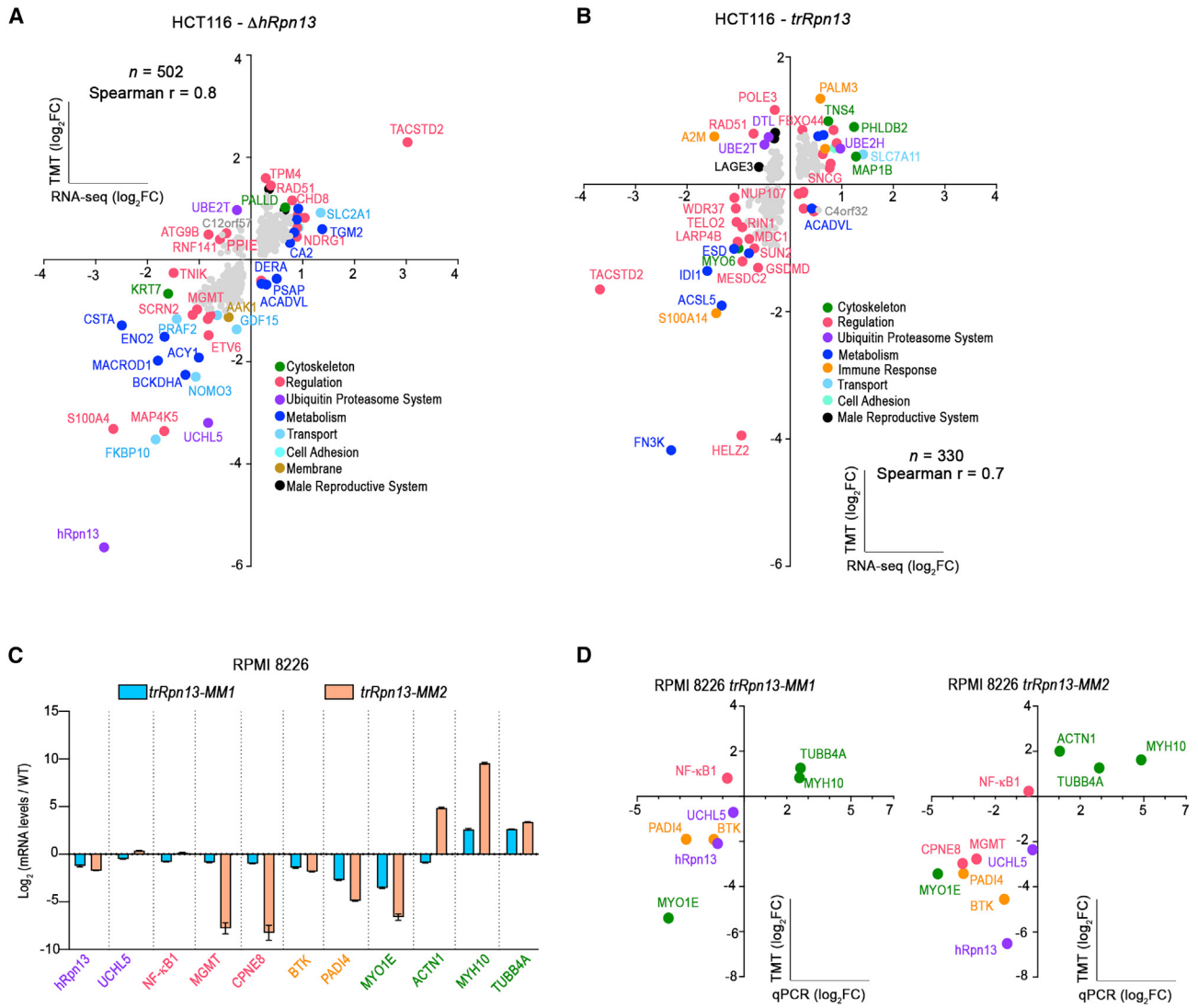

Figure 3. Proteome rewiring following hRpn13 or hRpn13 Pru loss correlates with mRNA changes

Plot of change in mRNA (x axis, log_2) versus protein (y axis, log_2) abundance in HCT116 *ΔhRpn13* (A and B) (A) and *trRpn13* (B) cells relative to *WT* for proteins with p value < 0.05. Spearman rank correlation and total number of proteins (n) is included.

(C) qPCR analysis as indicated in *trRpn13-MM1* or *trRpn13-MM2* relative to *WT*. Data are represented as mean ± SEM of three technical replicates.

(D) Plot of change in mRNA (x axis, log_2) versus protein (y axis, log_2) abundance in RPMI 8226 *trRpn13-MM1* (left) and *trRpn13-MM2* (right).

See also Figures S2 and S3.

proteins associated with immune response and reduced in *trRpn13-MM2* were not detected in the HCT116 *ΔhRpn13* or *trRpn13* cells (Figure S3). Neither was MAGEC2 or the solute carrier family 15 member 1 (SLC15A1), although MAGEC2 and SLC15A1 are present at low levels in the colon (ncbi.nlm.nih.gov; depmap.org).

We also analyzed the HCT116-edited lines by mRNA sequencing (mRNA-seq) (Illumina), plotting changes in mRNA versus protein abundance for *ΔhRpn13* and *trRpn13* (excluding p values > 0.05) and found strong correlation, with Spearman coefficients of 0.8 (Figure 3A) and 0.7 (Figure 3B), respectively. UCHL5 in *ΔhRpn13* notably deviated from this correlation, with a 10-fold protein loss but only 2-fold mRNA reduction (Figure 3A).

Lacking Illumina mRNA-seq data for *trRpn13-MM1/2* cells, we used qPCR to measure mRNA abundance for select gene products. UCHL5 expression was unperturbed; PADI4, MYO1E, and, to a lesser extent, BTK were reduced, while TUBB4A increased in both *trRpn13-MM1* and *trRpn13-MM2* (Figure 3C). MGMT and CPNE8 mRNA levels were reduced and ACTN1 increased in *trRpn13-MM2*, with only minor effects in *trRpn13-MM1* cells (Figure 3C), consistent with reduction of MGMT protein levels in *trRpn13-MM2* but not *trRpn13-MM1* cells (Figure 2C). MYH10 was increased in *trRpn13-MM1*, but with a pronounced effect in *trRpn13-MM2* (Figure 3C), where its protein abundance was increased (Figure 1B). A comparative plot of the qPCR and TMT-MS analyses for the respective cell lines revealed concordance

between transcriptomic and proteomic levels of the selected gene products (Figure 3D).

hRpn13 Pru deletion increases membrane blebbing in myeloma cells

To test whether the alterations of cytoskeletal protein abundance in *trRpn13-MM1* and *trRpn13-MM2* cells impacts cellular morphology, we used immunofluorescence staining and confocal microscopy visualizing F-actin by fluorescently labeled phalloidin (red), microtubules by dye-conjugated antibodies to TUBB4A (yellow), and DNA by DAPI (blue). *trRpn13-MM1* and *trRpn13-MM2* cells were similar morphologically to the parental cells, with a subset of each exhibiting a cell membrane blebbing phenotype in both interphase (Figure 4A, indicated by an arrow) and mitosis (Figure 4B). This phenotype, however, was significantly more frequent in *trRpn13-MM1/2* cells than in the parental cells (Figure 4C). To assess the contribution of programmed cell death to the blebbing phenotype, we stained *WT*, *trRpn13-MM1*, and *trRpn13-MM2* cells for the apoptotic marker Annexin V. In all cell lines, populations of apoptotic and non-apoptotic cells were observed with and without blebbing features (Figure 4D, blebbing indicated by an arrow). A subset of non-apoptotic *trRpn13-MM1/2* cells were also observed with large blebs (Figure 4D). It is possible that commonly altered cytoskeleton-associated proteins such as MYO1E, ACTL8, PDE5A,[31] SPART, or FMNL2 (Figures 1B, 2B, and 3D) contribute to the increased blebbing observed in *trRpn13-MM1/2* cells.

hRpn13 Pru binds and inhibits HDAC8

Because UCHL5 binds to hRpn13 DEUBAD, and MGMT responded similarly to UCHL5 following hRpn13-editing, we tested whether MGMT and hRpn13 interact in cells. We immunoprecipitated hRpn13 from RPMI 8226 lysates, but no co-immunoprecipitated MGMT was detected (data not shown). We previously developed a hRpn13-targeting PROTAC (XL5-VHL2) that causes reduced levels of $hRpn13^{Pru}$ in RPMI 8226 cells.[14] We tested whether XL5-VHL2-induced loss of $hRpn13^{Pru}$ alters MGMT abundance. RPMI 8226 *WT* or *trRpn13-MM2* cells were treated with 40 μM XL5-VHL2 or DMSO (vehicle control) for 24 h and the lysates immunoprobed for cleaved caspase-9 to measure apoptosis, hRpn13, MGMT, or β-actin (loading control). As expected, XL5-VHL2 induced apoptosis in *WT* cells, with loss of $hRpn13^{Pru}$ (Figure 5A, lane 3 compared with lane 1), whereas cleaved caspase-9 was barely detectable in XL5-VHL2-treated *trRpn13-MM2* cells (Figure 5A, lane 4 compared with lane 2). We further found reduced levels of MGMT in XL5-VHL2-treated *WT* cells (Figure 5A, lane 3 compared with lane 1); MGMT was not detected in *trRpn13-MM2* cells (Figure 5A, lanes 2 and 4), consistent with Figure 1D.

Over-expressed hRpn13 Pru domain interacts with HDAC8 in glioblastoma cells to impact HDAC8 regulation of MGMT expression.[29] We tested and found co-immunoprecipitation of HDAC8 with hRpn13 in HCT116, RPMI 8226, and the glioblastoma cell lines T98G and U87 (Figure 5B). MGMT is reduced in HCT116 and U87 cells compared with RPMI 8226 and T98G cells; however, the levels of HDAC8 that co-immunoprecipitated with hRpn13 were equivalent in RPMI 8226, T98G, and U87 cells (Figure 5B). Thus, MGMT abundance does not appear to impact hRpn13 interaction with HDAC8. Moreover, $hRpn13^{Pru}$ was not detected in T98G cells, where HDAC8 co-immunoprecipitated with hRpn13 (Figure 5B), indicating that full-length hRpn13 interacts with HDAC8 in T98G cells.

We hypothesized that the influence of hRpn13 over MGMT and PADI4 may be through direct binding to HDAC8. To test for direct interaction between hRpn13 Pru and HDAC8, we used 2D NMR. ^{15}N-labeled hRpn13 (1–150), which includes Pru, was incubated with unlabeled maltose-binding protein (MBP)-tagged HDAC8; MBP was used to increase HDAC8 solubility. Each protein was expressed and purified from *E. coli* and 9 μM unlabeled MBP-HDAC8 added to 9 μM ^{15}N-hRpn13 (1–150). Binding was tested by comparing 2D ^{1}H, ^{15}N heteronuclear single quantum coherence spectroscopy (HSQC) recordings using these mixtures to ^{15}N-hRpn13 (1–150) in the same buffer. Addition of MBP-HDAC8 caused loss of a subset of hRpn13 Pru signals, indicating binding (Figure 5C). Signal loss is caused by the large size of the protein complex, as MBP-HDAC8 is ~85 kDa. To preclude the possibility that MBP binds to hRpn13 Pru, we added 9 μM unlabeled MBP to 9 μM ^{15}N-hRpn13 (1–150) and acquired ^{1}H, ^{15}N HSQC data. Comparison with ^{15}N-hRpn13 (1–150) alone indicated no signal changes (Figure S4A). We conclude that the spectral changes observed with MBP-HDAC8 addition to ^{15}N-hRpn13 (1–150) were caused by HDAC8 binding to hRpn13 Pru.

We also tested whether MGMT binds to hRpn13 Pru by addition of 15 or 45 μM MGMT to 15 μM ^{15}N-hRpn13 (1–150), to find no spectral changes for hRpn13 signals in ^{1}H, ^{15}N HSQC spectra (Figures S4B–S4D). This finding is consistent with their lack of co-immunoprecipitation and indicates that hRpn13 Pru does not bind MGMT.

We used NMR chemical shift assignments from a previous study[17] to identify the hRpn13 amino acids impacted by HDAC8 binding (Figure 5C). Amino acids that were assigned and affected by HDAC8 were mapped onto the hRpn13 Pru:hRpn2 structure (Figure 5D). Although 10% of signals could not be assigned due to differences in buffer conditions required for HDAC8 solubility, residues that were assigned cluster at hRpn13 Pru surfaces used to bind hRpn2[15] or ubiquitin.[16] To test whether HDAC8 competes with hRpn2 for binding to hRpn13 Pru, 9 μM hRpn2 (940–953) was added to a pre-incubated complex of 9 μM ^{15}N-hRpn13 (1–150) and 9 μM MBP-HDAC8. hRpn2 (940–953) addition caused the hRpn13 Pru signals in a ^{1}H, ^{15}N HSQC spectrum to reappear at a location in the spectrum consistent with hRpn2 binding (Figures 5E and 5F; Figure 5C compared with Figure S5A), indicating that hRpn2 displaces HDAC8 from hRpn13 Pru.

We further assessed whether ubiquitin binding affects HDAC8 interaction with hRpn13 Pru. A ^{1}H, ^{15}N HSQC spectrum was acquired on a sample containing 18 μM ubiquitin mixed with pre-incubated 9 μM ^{15}N-hRpn13 (1–150) and 9 μM MBP-HDAC8. In contrast with hRpn2, hRpn13 Pru signals were not restored by ubiquitin addition (Figures S5B and S5C), indicating that ubiquitin does not prevent hRpn13 binding to HDAC8.

We next applied AlphaFold2-Multimer[32] or HDOCK[33] to model the hRpn13:HDAC8 complex. Whereas AlphaFold2-Multimer produced model structures that did not fit the NMR data (data not shown), HDOCK modeled HDAC8 to bind to hRpn13 amino acids that were attenuated by HDAC8 addition and that overlap with the hRpn2-binding surface (Figures S5D and S5E),

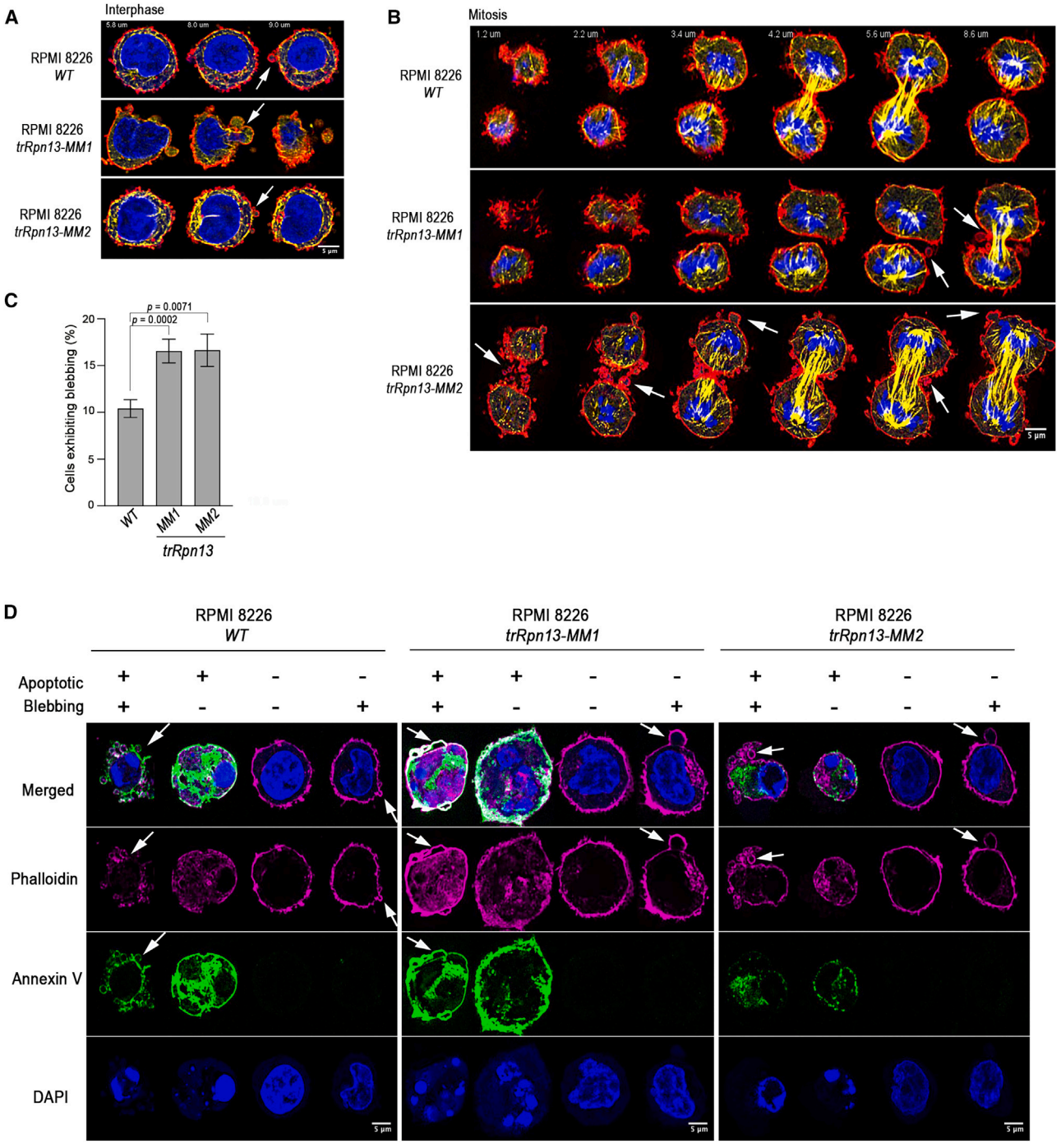

Figure 4. Membrane blebbing in myeloma cells is increased following hRpn13 Pru loss

(A and B) Slices from a confocal fluorescence microscopy z stack of representative RPMI 8226 *WT*, *trRpn13-MM1*, and *trRpn13-MM2* cells at interphase (A) or undergoing mitosis (B) stained for F-actin (phalloidin, red), β-tubulin (TUBB4A, yellow), and DNA (DAPI, blue). Membrane blebbing is indicated by white arrows. The distance from the cover glass for each slice (upper-left) and a scale bar (5 μm, bottom-right) are shown.

(C) Plot of percentage of blebbing cells as indicated. The Mann-Whitney non-parametric test was used to calculate statistical significance. Data are represented as mean ± SEM.

(D) Confocal fluorescence microscopy for RPMI 8226 *WT*, *trRpn13-MM1*, and *trRpn13-MM2* stained for Annexin V (green), F-actin (phalloidin, purple), and DNA (DAPI, blue). A merged view is included in the top panel and arrows indicate blebs. Scale bars are 5 μm.

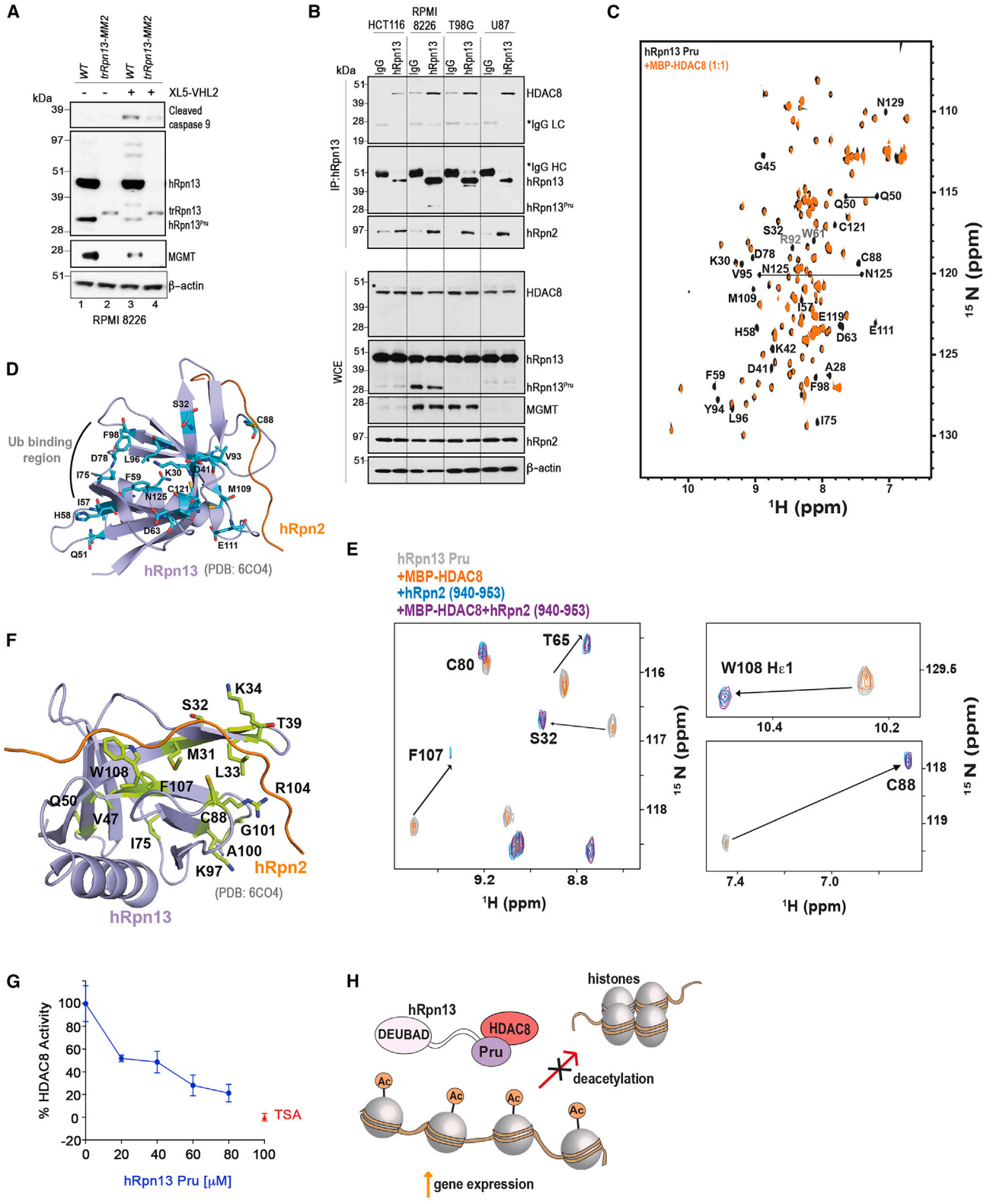

(legend on next page)

consistent with hRpn2 displacement of HDAC8 from hRpn13 (Figure 5E). This modeled structure, which is consistent with the experimental data, predicts hRpn13 to bind to the HDAC8 substrate interaction surface, suggesting that, like the HDAC8 inhibitor (HDAC8i) trichostatin A (TSA, PDB: 1T64),[34] hRpn13 inhibits HDAC8 activity by sterically preventing binding to substrates. To test directly whether hRpn13 inhibits HDAC8, we used a commercially available fluorogenic activity assay. We tested for HDAC8 activity with varying concentrations of hRpn13 (1–150) or TSA. As expected, TSA inhibited HDAC8, but so did hRpn13, with a concentration-dependent effect (Figure 5G). These data suggest that, in a cellular context, hRpn13 may allow expression of HDAC8-inhibited genes (Figure 5H), providing further explanation for how hRpn13 loss contributes to MGMT loss (Figure 2F), and supporting a model in which hRpn13 inhibits HDAC8 activity (Figure 5H).

hRpn13 binds PADI4 directly with co-immunoprecipitation from myeloma cells

We next examined the functional relationship between hRpn13 and the PADI enzyme family. mRNA-seq analyses revealed PADI4 and low levels of PADI2 mRNAs in RPMI 8226 cells, whereas PADI2 and PADI3 mRNAs were found in HCT116 cells (Figure S6A). We treated RPMI 8226 cells with 0, 5, 10, or 20 μM of a pan PADI inhibitor (pan-PADi) for 24 h and immunoprobed the cell lysates for hRpn13, HDAC8, MGMT, and markers of DNA damage or apoptosis. A concentration-dependent increase in DNA damage (γ-H2AX) and apoptosis (cleaved caspase-9) was observed, with a corresponding reduction of PADI4 and MGMT (Figure 6A). UCHL5 and full-length hRpn13 were unaffected; however, $hRpn13^{Pru}$ was reduced by treatment with 10 and 20 μM pan-PADi. To test for PADI4 specificity, we repeated this experiment with the PADI4-specific inhibitor GSK484 (PADI4i) to similarly find reduced levels of PADI4, MGMT, and $hRpn13^{Pru}$ with induction of apoptosis (Figure 6B).

We previously found the production of $hRpn13^{Pru}$ to be cell-type dependent.[14] To investigate this trend in the context of PADI4, we immunoprobed lysates from HCT116, RPMI 8226, cervical cancer HeLa, and immortalized human embryonic kidney HEK293T cells for PADI4, hRpn13, MGMT, HDAC8, and UCHL5. hRpn13 varied across the cell lines, with $hRpn13^{Pru}$ readily observed in RPMI 8226 cells, where PADI4 was also detected and UCHL5 increased (Figure 6C). Supporting a cell-type-dependent functional relationship, HDAC8 and MGMT levels were not correlated; MGMT was not observed in HEK293T cells where HDAC8 was elevated, but both proteins were reduced in HCT116 cells (Figure 6C). Moreover, treatment of HCT116 cells with pan-PADi, PADI4i, or hRpn13 PROTAC XL5-VHL2 did not induce apoptosis, in contrast with proteasome inhibitor carfilzomib (Figure S6B), providing further support for the cell-type specialization of PADI4 and $hRpn13^{Pru}$.

We next tested and found PADI4 to co-immunoprecipitate with hRpn13 from lysates of RPMI 8226 cells (Figure 6D, top); this interaction was not observed in HCT116 cells where, consistent with Figure 6C, PADI4 was not detected (Figure 6D, bottom). We used 2D NMR to test for direct interaction. Equimolar quantities of unlabeled PADI4 was added to 20 μM ^{15}N-hRpn13 (1–150) and a ^{1}H, ^{15}N HSQC spectrum acquired; for comparison, this experiment was performed without PADI4 and in identical buffer conditions. PADI4 caused the signals of residues G141, S143, and G144, present C-terminal to the hRpn13 Pru domain, to attenuate (Figures 6E and 6F). Spectral changes were also detected, which we hypothesized could be from hRpn13 arginine residues acting as substrates for PADI4, including attenuation of R16, which is within the N-terminal intrinsically disordered region, and of hRpn13 Pru residues C88, G91, and Q110, which are near R92, and C121 and N125 near R122 (Figures 6E and 6F).

PADI4 citrullinates hRpn13 Pru

To test whether hRpn13 (1–150) is citrullinated by PADI4, we incubated these two proteins together with either 10 mM $CaCl_2$ (to activate activity) or 5 mM EDTA (as a negative control). High-resolution MS was used to assay for arginine deimination, as this modification causes a molecular weight shift of +0.984 Da. We measured a molecular weight shift of 4 Da following incubation of hRpn13 (1–150) with PADI4 when $CaCl_2$ was present (Figure 6G, blue), suggesting the occurrence of four citrullination events; no such shift was detected with EDTA (Figure 6G, orange). hRpn13 R16 is within a "GSRG" sequence (Figure S6C), which is a proposed PADI4 citrullination motif.[35] We therefore tested whether this region might be one of the modified sites by incubating PADI4 with an hRpn13 peptide sequence that spans L11-N20 (LVPGSRGASN) with inclusion of either 10 mM $CaCl_2$ or 5 mM EDTA. This peptide was shifted by +0.984 Da with $CaCl_2$ and not EDTA, suggesting that R16 is

Figure 5. hRpn13 Pru binds and inhibits HDAC8

(A) Immunoblots of lysates from RPMI 8226 cells treated for 24 h with XL5-VHL2 (40 μM) or DMSO probed as indicated.

(B) Immunoblots of proteins immunoprecipitated with anti-hRpn13 antibodies (upper panels) and whole-cell extracts (WCEs, low panels) from HCT116, RPMI 8226, T98G, or U87 cells probed as indicated. An asterisk (*) indicates residual signal from probing hRpn13.

(C) ^{1}H, ^{15}N HSQC spectra of 9 μM ^{15}N-hRpn13 (1–150, black) and mixed with equimolar unlabeled MBP-HDAC8 (orange) at 25°C. Signals that attenuate upon addition of MBP-HDAC8 are labeled and sidechain NH_2 groups (Q50 and N125) that disappear are connected with a line.

(D) hRpn13 amino acids with signal broadening by adding MBP-HDAC8 are highlighted (cyan) and labeled on a ribbon diagram of hRpn13 Pru (purple):hRpn2 (940–953, light orange, PDB: 6CO4).

(E) ^{1}H, ^{15}N HSQC spectra of 9 μM ^{15}N-hRpn13 (1–150, gray) with equimolar unlabeled MBP-HDAC8 (9 μM, orange), equimolar unlabeled hRpn2 (940–953, 9 μM, cyan), or equimolar unlabeled MBP-HDAC8 and hRpn2 (940–953, 9 μM, purple). Signals that significantly disappear or shift are labeled.

(F) hRpn13 amino acids that shift or disappear upon addition of hRpn2 (940–953) to the hRpn13 and MBP-HDAC8 mixture are highlighted in green on a ribbon diagram of hRpn13 Pru (purple):hRpn2 (940–953, light orange, PDB: 6CO4).

(G) HDAC8 activity assay with indicated concentration (20, 40, 60, and 80 μM) of hRpn13 (1–150) or inhibitor TSA. Data are shown as mean ± SEM of three technical replicates.

(H) Model summarizing the inhibitory effect of hRpn13 on HDAC8 activity.

See also Figures S4 and S5.

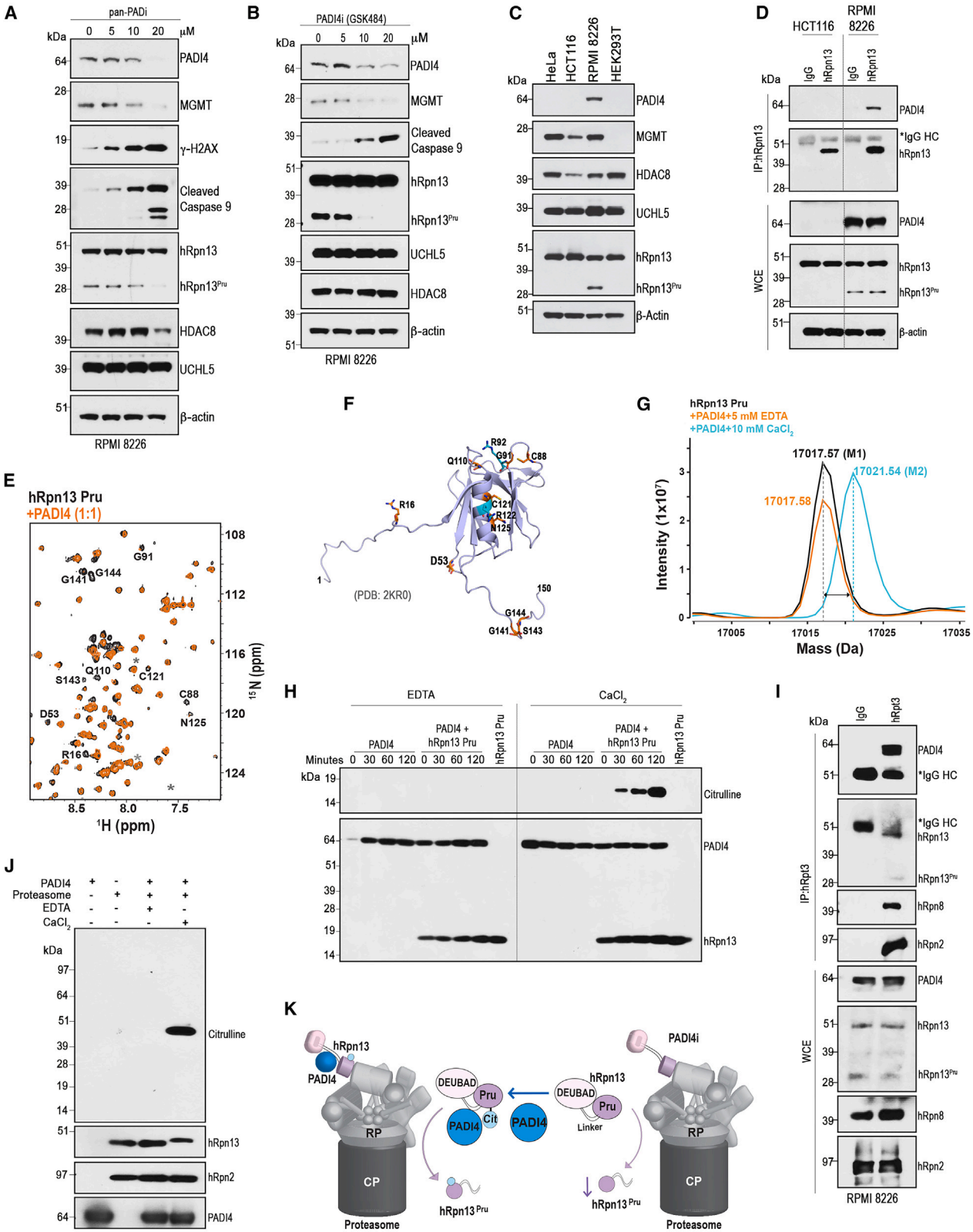

(legend on next page)

indeed citrullinated by PADI4 (Figure S6D). We further tested and found that amino acid substitution of R16 to alanine in hRpn13 (1–150) causes loss of one citrullination event (Figure S6E).

To validate the MS results of hRpn13 citrullination by PADI4, we used a commercially available kit for detecting citrullination. PADI4 alone or with hRpn13 (1–150) was dissolved in a buffer that contained EDTA or $CaCl_2$ and the reaction monitored by immunoblotting at 0, 30, 60, or 120 min. Antibodies against PADI4 and hRpn13 detected these proteins as expected (Figure 6H, lower panel). In addition, citrullination was detected only in the reactions that contained hRpn13 Pru and $CaCl_2$ (Figure 6H, upper panel).

Our data suggest that PADI4 binds to the intrinsically disordered region C-terminally adjacent to the hRpn13 Pru domain, and citrullinates hRpn13. In particular, PADI4 binds to a region that includes G141, S143 and G144 (Figure 6F), consistent with its interaction with disordered regions of histone proteins.[36] Further support for this model is present in the NMR data. In particular, PADI4 forms a dimer of ~148 kDa and, if hRpn13 Pru formed a stable complex with PADI4, then its signals would not be detectable under our experimental conditions due to the slow rotational correlation time of the large hRpn13 Pru:PADI4 complex and resulting fast NMR signal decay.[37] By contrast, interaction with one of the flexible intrinsically disordered regions at the terminal ends of the Pru domain would allow for its detection.

PADI4 binds and citrullinates 26S proteasomes

Because our NMR data suggest that PADI4 binds to a region of hRpn13 that does not overlap with its proteasome-binding site (Figures 6F vs. 5F), we hypothesized that PADI4 can bind to hRpn13 when assembled into the proteasome. Loss of hRpn13 causes loss of PADI4 (Figure 1B), and therefore we were unable to compare PADI4 levels at proteasomes, with and without hRpn13 present. Nonetheless, we performed a co-immunoprecipitation assay by using antibodies against hRpt3 (a proteasome ATPase subunit) for RPMI 8226 cells. PADI4 co-immunoprecipitated with hRpt3 along with hRpn13, hRpn8, and hRpn2 (Figure 6I), demonstrating that PADI4 is present at 26S proteasomes of RPMI 8226 cells. We next incubated PADI4 with commercial 26S proteasomes and immunoprobed for citrulline to find a single band between 39 and 51 kDa (Figure 6J), consistent with the modification of hRpn13, albeit also of other proteasome components.[38] Altogether, these data suggest a model in which PADI4 interaction with hRpn13 enables its interaction with proteasomes, where hRpn13 and potentially other proteasome subunits may be citrullinated by PADI4 and, moreover, PADI4 citrullination of hRpn13 may contribute to the production or stability of $hRpn13^{Pru}$ (Figure 6K).

Proteasome peptidase activity is reduced by treating myeloma cells with PADI4 inhibitor

We tested whether PADI4 impacts the chymotryptic activity of the proteasome core particle (CP) by subjecting the lysates of PADI4i-treated (10 μM for 24 h) RPMI 8226 cells (compared with DMSO vehicle control) to a fluorometric peptidase assay using a 7-amino-4-methylcoumarin (AMC)-tagged model substrate. A reduction in peptidase activity was measured for proteasomes from PADI4i-treated cells (Figure 7A). These data suggest that citrullination by PADI4 contributes to the peptidase activity of the 26S proteasome.

hRpn13 PROTAC XL5-VHL2 reduces MGMT, HDAC8, and PADI4 levels in myeloma cells

$hRpn13^{Pru}$ is generated by proteasomal cleavage of hRpn13 and is therefore reduced by proteasome inhibition.[14] We reasoned that if MGMT and PADI4 expression is linked to activities at the proteasome, then they would be sensitive to carfilzomib treatment. RPMI 8226 cells were treated with 40 μM XL5-VHL2, 30 μM HDAC8i, and 20 μM pan-PADi for 24 h and/or 250 nM carfilzomib for 12 h. The cell lysates from individual and/or combined inhibitor treatment were immunoprobed for PADI4, MGMT, HDAC8, UCHL5, hRpn13, γ-H2AX, NF-κB p50, NF-κB p65, bulk ubiquitin chains, and β-actin (as a loading control). As expected, XL5-VHL2 treatment resulted in reduced levels of $hRpn13^{Pru}$, with a concomitant decrease in PADI4, HDAC8, and MGMT (Figure 7B,

Figure 6. PADI4 binds and citrullinates hRpn13

(A and B) Lysates from RPMI 8226 *WT* cells treated for 24 h with pan-PADi (A, PAD CI-amidine) or PADI4i (B, GSK484) at 5, 10, or 20 μM concentration or DMSO (vehicle control) immunoprobed as indicated; γ-H2AX was also immunoprobed in (A).

(C) Lysates from HeLa, HCT116, RPMI 8226, or HEK293T cells immunoprobed as indicated.

(D) Immunoblots of proteins immunoprecipitated with anti-hRpn13 antibodies (top) and whole-cell extracts (WCEs, bottom) from HCT116 or RPMI 8226 cells, probed as indicated.

(E) ^{1}H, ^{15}N HSQC spectra of 20 μM ^{15}N-hRpn13 (1–150, black) alone or with equimolar unlabeled PADI4 (orange). Signals that disappear are labeled, whereas unassigned signals that disappeared are marked by asterisks.

(F) hRpn13 amino acids that shift or disappear upon addition of PADI4 are highlighted in orange on a ribbon diagram of hRpn13 Pru (gray, PDB: 2KR0), with Arg92 and Arg122 shown (cyan). The regions spanning 1–21 and 130–150 are intrinsically disordered, and this view represents one configuration from a dynamic ensemble.

(G) MS analysis of purified hRpn13 (1–150, black) alone and after 2 h incubation at 37°C with PADI4 with 5 mM EDTA (orange, as a control) or 10 mM $CaCl_2$ (blue). Detected masses are included.

(H) Immunoblots as indicated for PADI4 alone or mixed with hRpn13 (1–150) in 5 mM EDTA (left side, as control) or 10 mM $CaCl_2$ (right side) following 0, 30, 60, or 120 min of incubation.

(I) Immunoblots of proteins immunoprecipitated with anti-hRpt3 antibodies (top panels) and whole-cell extracts (WCEs, bottom) from RPMI 8226 cells probed as indicated.

(J) Immunoblots for reaction mixtures with combinations, as indicated of PADI4 (2,100 nM), 26S proteasome (100 nM), 5 mM EDTA, or 10 mM $CaCl_2$ for 120 min and probed as indicated.

(K) Model summarizing interactions between PADI4 (blue) and hRpn13 (shades of purple) or the 26S proteasome (shades of gray), the latter interaction hypothesized to be through hRpn13. PADI4 citrullinates hRpn13 (light blue, Cit) and PADI4i inhibition reduces $hRpn13^{Pru}$.

See also Figure S6.

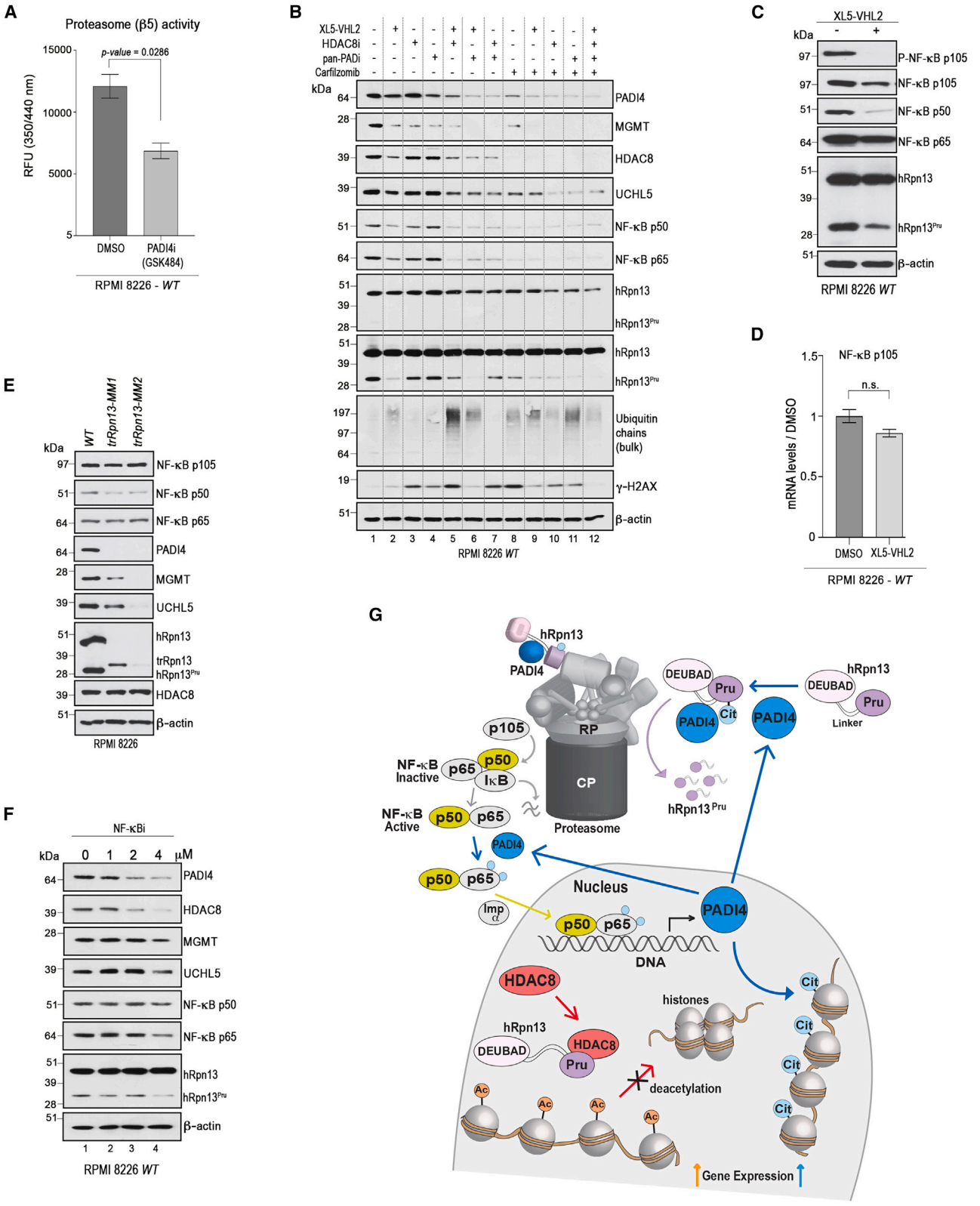

(legend on next page)

lane 2 versus 1). The levels of these proteins were drastically reduced in combined treatments of XL5-VHL2 with either HDAC8i or pan-PADi (Figure 7B, lanes 5, 6, or 7 versus 1). Carfilzomib caused notably decreased levels of PADI4, MGMT, HDAC8, UCHL5, (Figure 7B, lane 8) and, as expected,[14] hRpn13^{Pru}. Co-treatments led to greater depletion of these proteins (Figure 7B, lanes 9–12). Thus, an hRpn13^{Pru} PROTAC and proteasome inhibition each cause depletion of PADI4, HDAC8, and MGMT.

Reduced hRpn13 protein levels correlate with decreased NF-κB p50 levels

hRpn13[39] and PADI4[40] have been previously linked to NF-κB activity, with NF-κB p50—and to a lesser extent p65—present at the PADI4 promoter of TNF-α-treated HL-60 promyeoloblasts.[40] Moreover, PADI4 citrullinates NF-κB p65, inducing its interaction with importin α3 and, in turn, nuclear localization.[41] We immunoblotted lysates from RPMI 8226 cells treated with XL5-VHL2 with antibodies against NF-κB p50 and p65, to find their protein abundance reduced compared with vehicle control (Figure 7B, lane 2 versus 1). Co-treatment of XL5-VHL2 with either HDAC8i or pan-PADi, or HDAC8i combined with pan-PADi (Figure 7B, lanes 5–7), further reduced the levels of p50 and p65, which were barely detected in carfilzomib-treated cells (Figure 7B, lanes 8–12). Moreover, phosphorylated NF-κB p105 was depleted and p50 reduced in RPMI 8226 cells treated for 24 h with 40 μM XL5-VHL2 compared with DMSO vehicle control, with an apparent reduction of unmodified p105 and p65 (Figure 7C) and no change in the mRNA level of p105 (Figure 7D).

We further assayed the abundance of NF-κB p105, p50, and p65 in lysates from *trRpn13-MM1* or *trRpn13-MM2* compared with *WT* to find similar NF-κB p105 and p65 protein levels, but reduced p50 levels in the hRpn13-edited cell lines (Figure 7E). Notedly, the abundance of p50 in *trRpn13-MM1* was similar to in *trRpn13-MM2*, indicating the reduction to be caused specifically by loss of the hRpn13 Pru domain and/or hRpn13 activity at proteasomes.

We tested directly whether inhibition of NF-κB activity by the selective IκB kinase inhibitor BMS 345541 leads to reduced HDAC8 or PADI4 protein abundance. Lysates from RPMI 8226 cells treated with increasing concentration of BMS 345541 were immunoprobed, revealing a dose-dependent reduction in HDAC8 and PADI4 abundance (Figure 7F). At the highest concentration of 4 μM BMS 345541, UCHL5, MGMT, p65, and hRpn13^{Pru} were also decreased (Figure 7F, lane 4). Together with the finding that NF-κB transcription factors can interact with the PADI4 promoter,[40] our data suggest that the NF-κB pathway regulates expression of PADI4 in myeloma cells and, furthermore, that hRpn13 loss by either a PROTAC or gene editing causes reduced NF-κB p50 levels.

DISCUSSION

Our transcriptomic and proteomic data analyses following CRISPR-Cas9 deletion of hRpn13 or its Pru in two different cell types (HCT116 and RPMI 8226) indicate correlated alterations in the proteome and transcriptome, indicating that hRpn13 has profound effects that impact the molecular landscape beyond the proteasome. We report that hRpn13 interacts with epigenetic regulators of transcription, one of which (PADI4) is specific to bone marrow. Our findings thus implicate hRpn13 in cell-type-specific functions and indicate that it contributes to gene expression.

Whereas hRpn13 interaction with HDAC8 competes with hRpn2 and therefore occurs off proteasomes (Figure 5E), PADI4 binds at a region distinct from hRpn2 (Figures 5F and 6F). Therefore, hRpn13 may interact with PADI4 on or off proteasomes. We favor a model in which hRpn13 interacts with PADI4 at the proteasome, where it citrullinates hRpn13 (Figures 6J and 6K) and/or other proteasome subunits and thereby modulates proteasome activity (Figure 7A). Because hRpn13 expression in *trRpn13-MM2* recovered the low MYH10 levels of parental RPMI 8226 cells, but did not restore PADI4 levels, the mechanistic link between hRpn13 Pru deletion in *trRpn13-MM1/2* cells and PADI4 depletion is unclear. We find hRpn13 loss by gene editing leads to reduced NF-κB p50, with co-depletion of phosphorylated NF-κB p105 following hRpn13 PROTAC treatment. Moreover, inhibition of the NF-κB pathway causes PADI4 loss. Therefore, it is possible that the correlated loss of PADI4 with hRpn13 occurs through NF-κB. Moreover, the finding that citrullination of p65 promotes its interaction with importin α3 and trafficking into the nucleus[41] suggests that hRpn13^{Pru} citrullination may similarly induce its nuclear trafficking, where perhaps it inhibits deacetylation by HDAC8 and/or is more stable than in the cytosol, the latter hypothesis based on our finding that pan-PADI (Figure 6A) and PADI4i (Figure 6B) inhibition reduces hRpn13^{Pru} levels and the correlative increased abundance of hRpn13^{Pru} in PADI4-containing cell lines (Figure 6C).

Figure 7. Loss of hRpn13 reduces NF-κB p50 and NF-κB inhibition depletes HDAC8 and PADI4

(A) Chymotrypsin-like activity assay of proteasomes from RPMI 8226 cells treated with DMSO (vehicle control) or PADI4i (GSK484; 10 μM) for 24 h. RFU, relative fluorescence units; excitation/emission at 350/440. The Mann-Whitney non-parametric test was used to calculate statistical significance. Data are represented as mean ± SEM of four technical replicates.

(B) Lysates from RPMI 8226 cells treated for 24 h with XL5-VHL2 (40 μM), HDAC8i (PCI-34051; 30 μM), pan-PADi (PAD CI-amidine, 20 μM), or for 12 h with carfilzomib (250 nM), or DMSO immunoprobed as indicated.

(C) Lysates from RPMI 8226 cells treated with XL5-VHL2 (40 μM) for 24 h, or DMSO immunoprobed as indicated.

(D) qPCR analysis of NF-κB p105 mRNA levels in RPMI 8226 *WT* treated for 24 h with XL5-VHL2 (40 μM) or DMSO control. The Wilcoxon non-parametric test was used to calculate statistical significance. Data are represented as mean ± SEM of three technical replicates. n.s., not significant.

(E) Lysates from RPMI 8226 *WT*, *trRpn13-MM1*, or *trRpn13-MM2* cells were immunoprobed as indicated.

(F) Lysates from RPMI 8226 *WT* cells treated for 24 h with NF-κB inhibitor (NF-κBi; BMS-345541) at 1, 2, and 4 μM concentration or DMSO immunoprobed as indicated.

(G) Model summarizing the proposed regulatory relationships between the proteasome (shades of gray) and its subunit hRpn13 (Pru, lilac; DEUBAD, pink), HDAC8 (red), PADI4 (blue), and the NF-κB pathway (p105 and p65, gray, p50, green). Histones (gray), acetyl groups (Ac, orange), citrulline (Cit, light blue), and importin α3 (Imp α, gray) are included.

PADI4 inhibition delays progression of multiple myeloma[42] and, in myeloid cells, PADI4 mediates chromatin de-condensation during the innate immune response to infection.[43] It also regulates stem cell pluripotency during early embryogenesis by citrullination of core histones H3 and H4 as well as linker histone H1.[44] Thus, the loss of PADI4 by the hRpn13 PROTAC may contribute to induction of cell death in myeloma cells.

Because hRpn13 interacts with HDAC8 and PADI4 and influences NF-κB p50 levels, future studies are needed to test whether the observed effects on cytoskeletal or immune response proteins (Figure 1B) are direct and/or through these known transcriptional regulators. HDAC8 functions in the rearrangement of the cytoskeleton in myeloma cells[45] and perhaps hRpn13 Pru contributes to this activity. One phenotypic feature of cytoskeleton reorganization observed in the hRpn13-edited cell lines is increased cellular blebbing, namely membrane protrusions at the cell surface (Figures 4A and 4B). The commonly altered cytoskeleton-related proteins in *trRpn13-MM1* and *trRpn13-MM2* cells (Figure 2B) may have a downstream effect on the cells' structure that is yet to be studied. Principally associated with programmed cell death, blebbing also occurs in migrating or cytokinetic cells and acts as a survival mechanism for injured cells, which use blebbing to resist cell lysis.[46] Nevertheless, in the context of our study, blebbing could be part of a survival adaptation, possibly caused by altering the 26S proteasome degradation machinery.

MYH10 activity has recently been implicated in melanoma therapy resistance for tumor survival.[47] Moreover, silencing of MYH10 reduces cell migration and invasion in glioblastoma and hepatocellular carcinoma.[48,49] Depletion of hRpn13 induces MYH10, which is suppressed by re-expression of hRpn13 (Figure 2G), suggesting a role for hRpn13 in tumor survival through its regulation of MYH10.

In summary, our data suggest novel functions for hRpn13 in epigenetic regulation of gene expression through HDAC8 and PADI4 and also the intersection of these activities with the NF-κB pathway (Figure 7G). The importance of hRpn13 in transcriptional regulation and cellular rewiring provides new insights into its potential as an anti-cancer target. Moreover, we demonstrate the cell-type-specific arginine deiminase PADI4 to be present at proteasomes, indicating that proteasome constituency can vary by cell type, and future studies further investigating tissue-dependent proteasome variance will be highly informative in the context of proteasome-related pathologies and cell-type-specific therapies.

Limitations of the study

PADI4 is depleted by hRpn13 loss, challenging our efforts to directly test whether hRpn13 is required for PADI4 interaction with proteasomes, and further structural studies will be invaluable for mechanistically defining PADI4 activity at proteasomes. We found NF-κB inhibition to also reduce PADI4 levels and hRpn13 loss to correlate with reduced p50 abundance and depletion of phosphorylated p105, suggesting that hRpn13 may influence PADI4 abundance indirectly through the NF-κB pathway. Future studies testing whether loss of other proteasome substrate receptors similarly impact PADI4 abundance and/or the cytoskeletal effects observed with hRpn13 loss will be invaluable to dissecting hRpn13-specific effects from general proteasome defects. Moreover, the detection of citrullination in cells by MS is challenged by the common molecular weight shift for any deimination or deamination event and the limited sensitivity of available antibodies for citrullination. Similarly, evaluation of the function of hRpn13 in the cytoskeletal context was stymied by limited availability of commercial antibodies, including MYO1E. This study highlights the need for future experiments aimed at examining cell type and tissue variance of proteasome constituency and activity and, for hematological cells specifically, the functional interplay between proteasomes, hRpn13, PADI4, NF-κB signaling, and the cytoskeleton.

STAR★METHODS

Detailed methods are provided in the online version of this paper and include the following:

- KEY RESOURCES TABLE
- RESOURCE AVAILABILITY
  - Lead contact
  - Materials availability
  - Data and code availability
- EXPERIMENTAL MODEL AND STUDY PARTICIPANT DETAILS
  - *E. coli* strains
  - Mammalian cell culture
- METHOD DETAILS
  - Plasmids
  - Transfection and transduction experiments
  - Proteome and transcriptome analysis experiments
- CITRULLINATION ASSAYS
  - Citrullination detection by immunoblotting
  - Citrullination detection by mass spectrometry
- QUANTIFICATION AND STATISTICAL ANALYSIS

SUPPLEMENTAL INFORMATION

Supplemental information can be found online at https://doi.org/10.1016/j.molcel.2023.11.035.

ACKNOWLEDGMENTS

This work was supported in part by the Intramural Research Program of the National Cancer Institute (NCI), National Institutes of Health (NIH, 1 ZIA BC011490 and a FLEX award to K.J.W.) and in part by federal funds from the NCI, NIH under contract no. HHSN261201500003I and 75N91019D00024. We thank Dr. Christine Muli and Dr. Hitendra Negi for useful discussions regarding the proteasome activity measurements. We gratefully thank Janusz Koscielniak for his maintenance of the NMR spectrometers and the Optical Microscopy and Image Analysis Lab of NCI-Frederick for training and use of microscopes. This work utilized computational resources of the NIH HPC Biowulf cluster (http://hpc.nih.gov) and the Sequencing Facility Bioinformatics Group of the NCI. The content of this publication does not necessarily reflect the views or policies of the Department of Health and Human Services, nor does mention of trade names, commercial products, or organizations imply endorsement by the U.S. Government.

AUTHOR CONTRIBUTIONS

Conceptualization, K.J.W. and V.O.-A.; methodology, K.J.W and V.O.-A.; investigation, V.O.-A., M.C., X.L., V.M., S.D., T.A., M.D., C.F., Y.Z., M.E.C., and R.C.; resources, V.R.S. and R.E.S.; validation, V.O.-A. and M.C.; data curation, S.D., T.A., M.D., C.F., B.S., and Y.Z.; writing – original draft, K.J.W., V.O.-A., M.C., and X.L.; writing – review & editing, K.J.W., V.O.-A., M.C., and

X.L.; visualization, V.O.-A. and M.C.; project administration, K.J.W and V.O.-A.; supervision, K.J.W.

DECLARATION OF INTERESTS

The authors declare no competing interests.

INCLUSION AND DIVERSITY

We support inclusive, diverse, and equitable conduct of research. One or more of the authors of this paper self-identifies as an underrepresented ethnic minority in their field of research or within their geographical location. One or more of the authors of this paper self-identifies as a gender minority in their field of research.

Received: May 9, 2023
Revised: November 4, 2023
Accepted: November 27, 2023
Published: December 26, 2023

REFERENCES

1. Osei-Amponsa, V., and Walters, K.J. (2022). Proteasome substrate receptors and their therapeutic potential. Trends Biochem. Sci. *47*, 950–964.
2. Song, Y., Ray, A., Li, S., Das, D.S., Tai, Y.T., Carrasco, R.D., Chauhan, D., and Anderson, K.C. (2016). Targeting proteasome ubiquitin receptor Rpn13 in multiple myeloma. Leukemia *30*, 1877–1886.
3. Zheng, X., Guo, Y., Chen, Y., Chen, M., Lin, Z., Wu, Y., and Chen, Y. (2015). Knockdown of adhesion-regulating Molecule 1 inhibits proliferation in HL60 cells. Acta Haematol. *134*, 88–100.
4. Osei-Amponsa, V., Sridharan, V., Tandon, M., Evans, C.N., Klarmann, K., Cheng, K.T., Lack, J., Chari, R., and Walters, K.J. (2020). Impact of losing hRpn13 Pru or UCHL5 on proteasome clearance of ubiquitinated proteins and RA190 cytotoxicity. Mol. Cell. Biol. *40*, e00122-20.
5. Jang, S.H., Park, J.W., Kim, H.R., Seong, J.K., and Kim, H.K. (2014). ADRM1 gene amplification is a candidate driver for metastatic gastric cancers. Clin. Exp. Metastasis *31*, 727–733.
6. Fejzo, M.S., Anderson, L., von Euw, E.M., Kalous, O., Avliyakulov, N.K., Haykinson, M.J., Konecny, G.E., Finn, R.S., and Slamon, D.J. (2013). Amplification target ADRM1: role as an oncogene and therapeutic target for ovarian cancer. Int. J. Mol. Sci. *14*, 3094–3109.
7. Chen, W., Hu, X.T., Shi, Q.L., Zhang, F.B., and He, C. (2009). Knockdown of the novel proteasome subunit Adrm1 located on the 20q13 amplicon inhibits colorectal cancer cell migration, survival and tumorigenicity. Oncol. Rep. *21*, 531–537.
8. Yang, X., Miao, X., Wen, Y., Hu, J., Dai, W., and Yin, B. (2012). A possible connection between adhesion regulating molecule 1 overexpression and nuclear factor kappa B activity in hepatocarcinogenesis. Oncol. Rep. *28*, 283–290.
9. Yu, G.Y., Wang, X., Zheng, S.S., Gao, X.M., Jia, Q.A., Zhu, W.W., Lu, L., Jia, H.L., Chen, J.H., Dong, Q.Z., et al. (2018). RA190, a proteasome subunit ADRM1 inhibitor, suppresses intrahepatic cholangiocarcinoma by inducing NF-KB-mediated cell apoptosis. Cell. Physiol. Biochem. *47*, 1152–1166.
10. Trader, D.J., Simanski, S., and Kodadek, T. (2015). A reversible and highly selective inhibitor of the proteasomal ubiquitin receptor rpn13 is toxic to multiple myeloma cells. J. Am. Chem. Soc. *137*, 6312–6319.
11. Anchoori, R.K., Karanam, B., Peng, S., Wang, J.W., Jiang, R., Tanno, T., Orlowski, R.Z., Matsui, W., Zhao, M., Rudek, M.A., et al. (2013). A bis-benzylidine piperidone targeting proteasome ubiquitin receptor RPN13/ADRM1 as a therapy for cancer. Cancer Cell *24*, 791–805.
12. Anchoori, R.K., Jiang, R., Peng, S., Soong, R.S., Algethami, A., Rudek, M.A., Anders, N., Hung, C.F., Chen, X., Lu, X., et al. (2018). Covalent Rpn13-binding inhibitors for the treatment of ovarian cancer. ACS Omega *3*, 11917–11929.
13. Anchoori, R.K., Tan, M., Tseng, S.H., Peng, S., Soong, R.S., Algethami, A., Foran, P., Das, S., Wang, C., Wang, T.L., et al. (2020). Structure-function analyses of candidate small molecule RPN13 inhibitors with antitumor properties. PLoS One *15*, e0227727.
14. Lu, X., Sabbasani, V.R., Osei-Amponsa, V., Evans, C.N., King, J.C., Tarasov, S.G., Dyba, M., Das, S., Chan, K.C., Schwieters, C.D., et al. (2021). Structure-guided bifunctional molecules hit a DEUBAD-lacking hRpn13 species upregulated in multiple myeloma. Nat. Commun. *12*, 7318.
15. Lu, X., Nowicka, U., Sridharan, V., Liu, F., Randles, L., Hymel, D., Dyba, M., Tarasov, S.G., Tarasova, N.I., Zhao, X.Z., et al. (2017). Structure of the Rpn13-Rpn2 complex provides insights for Rpn13 and Uch37 as anticancer targets. Nat. Commun. *8*, 15540.
16. Husnjak, K., Elsasser, S., Zhang, N., Chen, X., Randles, L., Shi, Y., Hofmann, K., Walters, K.J., Finley, D., and Dikic, I. (2008). Proteasome subunit Rpn13 is a novel ubiquitin receptor. Nature *453*, 481–488.
17. Schreiner, P., Chen, X., Husnjak, K., Randles, L., Zhang, N., Elsasser, S., Finley, D., Dikic, I., Walters, K.J., and Groll, M. (2008). Ubiquitin docking at the proteasome through a novel pleckstrin-homology domain interaction. Nature *453*, 548–552.
18. Lu, X., Ebelle, D.L., Matsuo, H., and Walters, K.J. (2020). An extended conformation for K48 ubiquitin chains revealed by the hRpn2:Rpn13:K48-Diubiquitin structure. Structure *28*, 495–506.e3.
19. Lu, X., Liu, F., Durham, S.E., Tarasov, S.G., and Walters, K.J. (2015). A high affinity hRpn2-derived peptide that displaces human Rpn13 from proteasome in 293T cells. PLoS One *10*, e0140518.
20. VanderLinden, R.T., Hemmis, C.W., Yao, T., Robinson, H., and Hill, C.P. (2017). Structure and energetics of pairwise interactions between proteasome subunits RPN2, RPN13, and ubiquitin clarify a substrate recruitment mechanism. J. Biol. Chem. *292*, 9493–9504.
21. Hamazaki, J., Iemura, S., Natsume, T., Yashiroda, H., Tanaka, K., and Murata, S. (2006). A novel proteasome interacting protein recruits the deubiquitinating enzyme UCH37 to 26S proteasomes. EMBO J. *25*, 4524–4536.
22. Yao, T., Song, L., Xu, W., DeMartino, G.N., Florens, L., Swanson, S.K., Washburn, M.P., Conaway, R.C., Conaway, J.W., and Cohen, R.E. (2006). Proteasome recruitment and activation of the Uch37 deubiquitinating enzyme by Adrm1. Nat. Cell Biol. *8*, 994–1002.
23. Qiu, X.B., Ouyang, S.Y., Li, C.J., Miao, S., Wang, L., and Goldberg, A.L. (2006). hRpn13/ADRM1/GP110 is a novel proteasome subunit that binds the deubiquitinating enzyme, UCH37. EMBO J. *25*, 5742–5753.
24. Deol, K.K., Crowe, S.O., Du, J., Bisbee, H.A., Guenette, R.G., and Strieter, E.R. (2020). Proteasome-bound UCH37/UCHL5 debranches ubiquitin chains to promote degradation. Mol. Cell *80*, 796–809.e9.
25. Chen, X., Lee, B.H., Finley, D., and Walters, K.J. (2010). Structure of proteasome ubiquitin receptor hRpn13 and its activation by the scaffolding protein hRpn2. Mol. Cell *38*, 404–415.
26. Palombella, V.J., Rando, O.J., Goldberg, A.L., and Maniatis, T. (1994). The ubiquitin-proteasome pathway is required for processing the NF-kappa B1 precursor protein and the activation of NF-kappa B. Cell *78*, 773–785.
27. Randles, L., Anchoori, R.K., Roden, R.B., and Walters, K.J. (2016). The proteasome ubiquitin receptor hRpn13 and its interacting deubiquitinating enzyme Uch37 are required for proper cell cycle progression. J. Biol. Chem. *291*, 8773–8783.
28. Doyle, J.M., Gao, J., Wang, J., Yang, M., and Potts, P.R. (2010). MAGE-RING protein complexes comprise a family of E3 ubiquitin ligases. Mol. Cell *39*, 963–974.
29. Santos-Barriopedro, I., Li, Y., Bahl, S., and Seto, E. (2019). HDAC8 affects MGMT levels in glioblastoma cell lines via interaction with the proteasome receptor ADRM1. Genes Cancer *10*, 119–133.
30. Song, Y., Du, T., Ray, A., Chauhan, K., Samur, M., Munshi, N., Chauhan, D., and Anderson, K.C. (2021). Identification of novel anti-tumor therapeutic target via proteomic characterization of ubiquitin receptor ADRM1/Rpn13. Blood Cancer J. *11*, 13.

31. Arozarena, I., Sanchez-Laorden, B., Packer, L., Hidalgo-Carcedo, C., Hayward, R., Viros, A., Sahai, E., and Marais, R. (2011). Oncogenic BRAF induces melanoma cell invasion by downregulating the cGMP-specific phosphodiesterase PDE5A. Cancer Cell *19*, 45–57.

32. Jumper, J., Evans, R., Pritzel, A., Green, T., Figurnov, M., Ronneberger, O., Tunyasuvunakool, K., Bates, R., Žídek, A., Potapenko, A., et al. (2021). Highly accurate protein structure prediction with AlphaFold. Nature *596*, 583–589.

33. Yan, Y., Zhang, D., Zhou, P., Li, B., and Huang, S.Y. (2017). HDOCK: a web server for protein-protein and protein-DNA/RNA docking based on a hybrid strategy. Nucleic Acids Res. *45*, W365–W373.

34. Somoza, J.R., Skene, R.J., Katz, B.A., Mol, C., Ho, J.D., Jennings, A.J., Luong, C., Arvai, A., Buggy, J.J., Chi, E., et al. (2004). Structural snapshots of human HDAC8 provide insights into the class I histone deacetylases. Structure *12*, 1325–1334.

35. Tanikawa, C., Ueda, K., Suzuki, A., Iida, A., Nakamura, R., Atsuta, N., Tohnai, G., Sobue, G., Saichi, N., Momozawa, Y., et al. (2018). Citrullination of RGG motifs in FET proteins by PAD4 regulates protein aggregation and ALS susceptibility. Cell Rep. *22*, 1473–1483.

36. Arita, K., Shimizu, T., Hashimoto, H., Hidaka, Y., Yamada, M., and Sato, M. (2006). Structural basis for histone N-terminal recognition by human peptidylarginine deiminase 4. Proc. Natl. Acad. Sci. USA *103*, 5291–5296.

37. Walters, K.J., Ferentz, A.E., Hare, B.J., Hidalgo, P., Jasanoff, A., Matsuo, H., and Wagner, G. (2001). Characterizing protein-protein complexes and oligomers by nuclear magnetic resonance spectroscopy. Methods Enzymol. *339*, 238–258.

38. Negi, H., Osei-Amponsa, V., Ibrahim, B., Evans, C.N., Sullenberger, C., Loncarek, J., Chari, R., and Walters, K.J. (2023). An engineered cell line with a hRpn1-attached handle to isolate proteasomes. J. Biol. Chem. *299*, 104948.

39. Mazumdar, T., Gorgun, F.M., Sha, Y., Tyryshkin, A., Zeng, S., Hartmann-Petersen, R., Jørgensen, J.P., Hendil, K.B., and Eissa, N.T. (2010). Regulation of NF-kappaB activity and inducible nitric oxide synthase by regulatory particle non-ATPase subunit 13 (Rpn13). Proc. Natl. Acad. Sci. USA *107*, 13854–13859.

40. Abbas, A.K., Le, K., Pimmett, V.L., Bell, D.A., Cairns, E., and Dekoter, R.P. (2014). Negative regulation of the peptidylarginine deiminase type IV promoter by NF-κB in human myeloid cells. Gene *533*, 123–131.

41. Sun, B., Dwivedi, N., Bechtel, T.J., Paulsen, J.L., Muth, A., Bawadekar, M., Li, G., Thompson, P.R., Shelef, M.A., Schiffer, C.A., et al. (2017). Citrullination of NF-κB p65 promotes its nuclear localization and TLR-induced expression of IL-1β and TNFα. Sci. Immunol. *2*, eaal3062.

42. Li, M., Lin, C., Deng, H., Strnad, J., Bernabei, L., Vogl, D.T., Burke, J.J., and Nefedova, Y. (2020). A novel peptidylarginine deiminase 4 (PAD4) inhibitor BMS-P5 blocks formation of neutrophil extracellular traps and delays progression of multiple myeloma. Mol. Cancer Ther. *19*, 1530–1538.

43. Neeli, I., Khan, S.N., and Radic, M. (2008). Histone deimination as a response to inflammatory stimuli in neutrophils. J. Immunol. *180*, 1895–1902.

44. Christophorou, M.A., Castelo-Branco, G., Halley-Stott, R.P., Oliveira, C.S., Loos, R., Radzisheuskaya, A., Mowen, K.A., Bertone, P., Silva, J.C.R., Zernicka-Goetz, M., et al. (2014). Citrullination regulates pluripotency and histone H1 binding to chromatin. Nature *507*, 104–108.

45. Chyra, Z., Gkotzamanidou, M., Shammas, M.A., Souliotis, L.V., Xu, Y., Samur, M.K., Beeler, A.B., Hajek, R., Fulciniti, M., and Munshi, N.C. (2019). HDAC8 maintain cytoskeleton integrity via homologous recombination and represent a novel therapeutic target in multiple myeloma. Blood *134*, 4385.

46. Babiychuk, E.B., Monastyrskaya, K., Potez, S., and Draeger, A. (2011). Blebbing confers resistance against cell lysis. Cell Death Differ. *18*, 80–89.

47. Orgaz, J.L., Crosas-Molist, E., Sadok, A., Perdrix-Rosell, A., Maiques, O., Rodriguez-Hernandez, I., Monger, J., Mele, S., Georgouli, M., Bridgeman, V., et al. (2020). Myosin II reactivation and cytoskeletal remodeling as a hallmark and a vulnerability in melanoma therapy resistance. Cancer Cell *37*, 85–103.e9.

48. Wang, Y., Yang, Q., Cheng, Y., Gao, M., Kuang, L., and Wang, C. (2018). Myosin heavy chain 10 (MYH10) gene silencing reduces cell migration and invasion in the glioma cell lines U251, T98G, and SHG44 by inhibiting the Wnt/β-catenin pathway. Med. Sci. Monit. *24*, 9110–9119.

49. Jin, Q., Cheng, M., Xia, X., Han, Y., Zhang, J., Cao, P., and Zhou, G. (2021). Down-regulation of MYH10 driven by chromosome 17p13.1 deletion promotes hepatocellular carcinoma metastasis through activation of the EGFR pathway. J. Cell. Mol. Med. *25*, 11142–11156.

50. Gibson, D.G., Young, L., Chuang, R.Y., Venter, J.C., Hutchison, C.A., and Smith, H.O. (2009). Enzymatic assembly of DNA molecules up to several hundred kilobases. Nat. Methods *6*, 343–345.

STAR★METHODS

KEY RESOURCES TABLE

REAGENT or RESOURCE	SOURCE	IDENTIFIER
Antibodies		
Rabbit anti-ADRM1 (hRpn13)	Abcam	Cat#ab157185; RRID: AB_2857945
Rabbit anti-UCHL5	Abcam	Cat#ab133508; RRID: AB_2814821
Rabbit anti HDAC8	Abcam	Cat#ab187139; RRID: AB_2715505
Rabbit anti-Rpn2	Abcam	Cat#ab2941; RRID: AB_2237798
Rabbit anti-Rpt3	Abcam	Cat# ab140515
Rabbit anti-Rpn8	Abcam	Cat# ab140428
Mouse anti-PADI4	Abcam	Cat#ab128086; RRID: AB_11140412
Rabbit anti-MYH10	Abcam	Cat#ab230823
Rabbit anti-TUBB4A	Abcam	Cat#ab179509; RRID: AB_2716759
Veriblot IP detection HRP-reagent	Abcam	Cat# ab131366; RRID: AB_2892718
Mouse anti-ubiquitin	Cell Signaling Technology	Cat#3936; RRID: AB_331292
Rabbit anti-MGMT	Cell Signaling Technology	Cat#2739; RRID: AB_2297658
Rabbit anti-NF-κB p105/p50	Cell Signaling Technology	Cat#13586; RRID: AB_2665516
Rabbit anti-NF-κB p65	Cell Signaling Technology	Cat#8242; RRID: AB_10859369
Rabbit anti-Phosphorylated NF-κB p105	Cell Signaling Technology	Cat#4806; RRID: AB_2282911
Rabbit anti-Cleaved Caspase 9	Cell Signaling Technology	Cat#52873; RRID: AB_2799423
Rabbit anti-NF-κB p105/p50	Abcam	Cat#ab32360
Rabbit anti-NF-κB p105	Cell Signaling Technology	Cat#4717; RRID: AB_2282895
Rabbit anti-TACSTD2	Cell Signaling Technology	Cat#90540; RRID: AB_2800160
Rabbit anti-β-actin	Cell Signaling Technology	Cat#4970; RRID: AB_2223172
Rabbit anti-S100A14	Proteintech Group Inc	Cat#10489-1-AP; RRID: AB_2183628
Rabbit anti-PADI4	Proteintech Group Inc	Cat#17373-1-AP; RRID: AB_2878398
Rabbit IgG HRP-conjugated	Thermo Fisher Scientific	Cat#A16110; RRID: AB_2534782
Mouse IgG HRP-conjugated	Sigma	Cat# A9917; RRID: AB_258476
Anti-Citrulline (Modified) Detection Kit	Sigma	Cat#17-347B
Bacterial and virus strains		
Escherichia coli BL21(DE3)	Invitrogen	C600003
Escherichia coli BL21(DE3) pLysS	Invitrogen	C606003
Chemicals, peptides, and recombinant proteins		
Sequencing Grade Modified Trypsin	Promega Corporation	Cat#V51111
TMTpro™ 16plex Label Reagent Set	Thermo Fisher Scientific	Cat#A44520
Pierce™ BCA Protein Assay Kit	Thermo Fisher Scientific	Cat#23225
Pierce ECL chemiluminescent reagents	Thermo Fisher Scientific	Cat#32106
PreScission protease	GE Healthcare Life Sciences	Cat#GE27-0843-01
Mini protease inhibitor cocktail	Roche	Cat#11836153001
Protease inhibitor cocktail	Roche	Cat#04693759001
PhosSTOP	Roche	Cat#4906837001
Phenylmethylsulfonyl fluoride (PMSF)	MP Biomedicals	Cat#195381
Tris(2-carboxyethyl)phosphine hydrochloride (TCEP)	Thermo Fisher Scientific	Cat#20491
Adenosine 5′-triphosphate disodium salt hydrate	Sigma	Cat# 34369-07-8
Isopropyl-1-thio-β-D-thiogalactopyranoside (IPTG)	UBPBio	Cat#P1010-10
XL5-VHL2	Lu et al.[14]	N/A
Carfilzomib	Selleck Chemicals LLC	Cat#S2853

(*Continued on next page*)

Continued

REAGENT or RESOURCE	SOURCE	IDENTIFIER
BMS 345541 (NFκB inhibitor)	Selleck Chemicals LLC	Cat#S8044
PAD CI-amidine	Sigma	Cat#506282
GSK484 (PADI4 specific inhibitor)	Abcam	Cat#ab223598
GSK484 (PADI4 specific inhibitor)	Cayman Chemical Co Inc	Cat#17488
Lipofectamine™ 3000 Reagent	Thermo Fisher Scientific	Cat# L3000015
Lipofectamine™ 2000 Reagent	Thermo Fisher Scientific	Cat# 11668027
Opti-MEM®	Life Technologies	Cat#31985070
37% formaldehyde	Electron Microscopy Science	Cat#15686
DAPI nuclear stain	Thermo Fisher Scientific	Cat#D1306
Phalloidin ATTO643 fluorescent dye	ATT0-TEC	Cat#AD643-81
Poly-L-lysine	Sigma	Cat#P8920
Mounting Medium	Biotium	Cat#23008
Dynabead protein G	Thermo Fisher Scientific	Cat#10004
RNeasy Plus mini kit	Qiagen	Cat#74134
High capacity RNA-to-cDNA kit	Applied Biosystem	Cat#04387406
McCoy's 5A (modified) media	Thermo Fisher Scientific	Cat#16600082
RPMI-1640 media	American Tissue Culture Collection	Cat#30-2001
EMEM media	American Tissue Culture Collection	Cat#30-2003
DMEM (GlutaMAX) media	Thermo Fisher Scientific	Cat#10566016
Proteasome 26S (human), (purified)	Enzo Life Science	Cat# BML-PW9310-0050
Critical commercial assays		
HDAC8 Fluorogenic Assay Kit	BPS Bioscience	Cat#50068
EasyPep™ MS Sample Prep Kits	Thermo Fisher Scientific	Cat#A45735
EasyPep™ MS Sample Prep Kits	Thermo Fisher Scientific	Cat#A40006
ProNex® Size-Selective Purification System	Promega Corporation	Cat#NG2003
TruSeq Stranded Total RNA kit	Illumina	Cat#RS-122-2201
Biotium Mix-n-Stain Kit for CF488A	Biotium	Cat#92253
Biotium Mix-n-Stain Kit for CF568	Biotium	Cat#92255
Annexin V – CF488A Conjugates	Biotium	Cat#29005
Genejet Endo-Free Plasmid Maxiprep kit	Thermo Fisher Scientific	Cat#K0861
Fluorometric Proteasome Activity Assay Kit	Abcam	Cat#ab107921
Deposited data		
NMR solution structure of hRpn13 Pru:hRpn2	Lu et al.[15]	PDB: 6CO4
NMR solution structure of hRpn13	Chen et al.[25]	PDB: 2RK0
TMT-MS data for RPMI 8226 parental and trRpn13-MM2, HCT116 parental, ΔhRpn13, and trRpn13	This study	MassIVE: MSV000091862
TMT-MS data for RPMI 8226 trRpn13-MM1	This study	MassIVE: MSV000093091
RNA-seq Illumina data for HCT116 ΔhRpn13	This study	NCBI BioProject: SAMN34603004
RNA-seq Illumina data for HCT116 ΔhRpn13	This study	NCBI BioProject: SAMN34603005
RNA-seq Illumina data for HCT116 ΔhRpn13	This study	NCBI BioProject: SAMN34603006
RNA-seq Illumina data for HCT116 parental	This study	NCBI BioProject: SAMN34603007
RNA-seq Illumina data for HCT116 parental	This study	NCBI BioProject: SAMN34603008
RNA-seq Illumina data for HCT116 parental	This study	NCBI BioProject: SAMN34603009
RNA-seq Illumina data for HCT116 parental	This study	NCBI BioProject: SAMN34603010
RNA-seq Illumina data for HCT116 parental	This study	NCBI BioProject: SAMN34603011
RNA-seq Illumina data for HCT116 parental	This study	NCBI BioProject: SAMN34603012
RNA-seq Illumina data for HCT116 trRpn13	This study	NCBI BioProject: SAMN34603013
RNA-seq Illumina data for HCT116 trRpn13	This study	NCBI BioProject: SAMN34603014

(*Continued on next page*)

Continued

REAGENT or RESOURCE	SOURCE	IDENTIFIER
RNA-seq Illumina data for HCT116 trRpn13	This study	NCBI BioProject: SAMN34603015
Original data for immunoblots	This study	Mendeley Data: https://doi.org/10.17632/cs84mzcrbr.1
Original data for confocal microscopy	This study	Mendeley Data: https://doi.org/10.17632/gr2994bzky.1
Experimental models: Cell lines		
Human: RPMI 8226 multiple myeloma cell line	American Tissue Culture Collection	CRM-CCL-155
Human: HCT116 colorectal cancer cell line	American Tissue Culture Collection	CCL-247
Human: T98G glioblastoma cell line	American Tissue Culture Collection	CRL-1690
Human: U87 glioblastoma cell line	American Tissue Culture Collection	HTB-14
Oligonucleotides		
TaqMan probe for UCHL5	Applied Biosystem	Hs01044470_m1
TaqMan probe for hRpn13	Applied Biosystem	Hs00544115_m1
TaqMan probe for MGMT	Applied Biosystem	Hs01037698_m1
TaqMan probe for PADI4	Applied Biosystem	Hs01057483_m1
TaqMan probe for CPNE8	Applied Biosystem	Hs01040084_m1
TaqMan probe for MYO1E	Applied Biosystem	Hs00192232_m1
TaqMan probe for MYH10	Applied Biosystem	Hs00992055_m1
TaqMan probe for ACTN1	Applied Biosystem	Hs00998100_m1
TaqMan probe for TUBB4A	Applied Biosystem	Hs00760066_s1
TaqMan probe for BTK	Applied Biosystem	Hs00975865_m1
TaqMan probe for GAPDH	Applied Biosystem	Hs99999905_m1
TaqMan probe for β-actin	Applied Biosystem	Hs99999903_m1
TaqMan probe for NF-κB1	Applied Biosystem	Hs00765730_m1
TaqMan probe for 18S: Forward: CTGAGAAACGGCTACCACATC Reverse: GCCTCGAAAGAGTCCTGTATTG Probe: AAATTACCCACTCCCGACCCGG	This paper	Customized from Integrated DNA Technology (IDT)
LVPGSRGASN	This study	Customized from GenScript
ON-TARGET plus siRNA against hRpn13	Dharmacon	LQ-012340-01-0005
Scrambled non-targeting pool siRNA	Dharmacon	D-001810-10-05
Recombinant DNA		
His-MBP-TEV-HDAC8	Addgene	Plasmid#122174
pGEX-6P-1-MGMT-GST	This study	Customized from GenScript
pGEX-6P-1-PADI4-GST	This study	Customized from GenScript
pGEX-6P-1-hRpn13 Pru R16A-GST	This study	Customized from GenScript
hRpn2 (940 – 953)	Lu et al.[15]	N/A
hRpn13 Pru (1 – 150)	Lu et al.[14]	N/A
pCMV-3Tag-1A-FLAG-hRpn13	This study	Customized from GenScript
pGMC00021	Addgene	Plasmid#195305
pMG0784 (cDNA hRpn13)	This study	Plasmid#210768
psPAX2	Addgene	Plasmid#12260
pMD.2G	Addgene	Plasmid#12259
Software and algorithms		
Andor Fusion software	Oxford Instruments	N/A
Mass Hunter Workstation	Agilent	N/A
Python	Python Software Foundation	N/A
R programming	The R Project for Statistical Computing	N/A
Limma package	Bioconductor	N/A

(*Continued on next page*)

Continued

REAGENT or RESOURCE	SOURCE	IDENTIFIER
GraphPad Prism	Dotmatics	N/A
Database for Annotation, Visualization and Integrated Discovery (DAVID)	National Institute of Health	N/A
HDOCK server	Yan et al.[33]	N/A
Other		
Iso-Seq™ Express Template Preparation protocol	Pacific Biosciences	PN 101-763-800
0.45 μm PDVF membrane	Merck Millipore	Cat#IPVH85R
0.2 μm PDVF membrane	Merck Millipore	Cat#ISEQ85R
Millipore Steriflip 0.45 μm	Merck Millipore	Cat#SE1M003M00
LentiX Concentrator	Takara	Cat#631232

RESOURCE AVAILABILITY

Lead contact

Further information and requests for resources and reagents should be directed to and will be fulfilled by the lead contact, Kylie J. Walters (kylie.walters@nih.gov).

Materials availability

Plasmids used in this study were customized and generated by GenScript.

Material availability requests should be made to the lead contact, Kylie J. Walters (kylie.walters@nih.gov).

Data and code availability

- The original TMT-MS data have been deposited at MassIVE and are publicly available as of the date of publication with project accession number MSV000091862 (for RPMI 8226 parental and *trRpn13-MM2*, HCT116 parental, *ΔhRpn13*, and *trRpn13* cells) and MSV000093091 (for RPMI 8226 trRpn13-MM1). The original RNA-sequencing data are deposited at NCBI BioProject with accession codes SAMN34603004-6 (for HCT116 *ΔhRpn13* cells), SAMN34603007-12 (for HCT116 parental cells) and SAMN34603013-15 (for HCT116 *trRpn13* cells). The original data for immunoblots and confocal microscopy are deposited at Mendeley (https://doi.org/10.17632/cs84mzcrbr.1 for blots; https://doi.org/10.17632/gr2994bzky.1 for microscopy images).
- This paper does not report original code.
- Any additional information required to reanalyze the data reported in this paper is available from the lead contact upon request.

EXPERIMENTAL MODEL AND STUDY PARTICIPANT DETAILS

E. coli strains

BL21 (DE3) and pLysS (DE3) cells were used in this study for the production of recombinant proteins.

Mammalian cell culture

HCT116, RPMI 8226, T98G, U87, HeLa, and HEK293T cells were obtained from American Tissue Culture Collection (ATCC) and cultured at 37°C in a humidified environment of 5% CO_2 in McCoy's 5A modified, RPMI-1640, EMEM, and DMEM (GlutaMAX) media, respectively (ATCC) and supplemented with 10% fetal bovine serum (Atlanta Biologicals). HCT116 *ΔhRpn13* cells were a gift from Shigeo Murata; HCT116 *trRpn13* and RPMI-8226 *trRpn13-MM1* and *trRpn13-MM2* cells were generated by CRISPR/Cas9 editing, as previously described.[4,14]

METHOD DETAILS

Plasmids

A plasmid for expressing His-MBP-TEV-HDAC8 that contains HDAC8 amino acids 8–374 was purchased from Addgene. hRpn13 (1-150) Pru R16A, MGMT (1–207) and PADI4 (1–663) were subcloned into the pGEX-6P-1 vector in frame and C-terminal to glutathione-S-transferase and an intervening PreScission protease recognition sequence with codon optimization (GenScript), as was hRpn2 (940–953) for a previous study.[15] hRpn13 Pru (1–150) was in frame with an N-terminal histidine tag and intervening PreScission

protease recognition site, as previously described.[14] *ADRM1* cDNA was cloned in frame with an N-terminal FLAG (x3) tag into a pCMV-3Tag-1 vector (FLAG-hRpn13) customized from GenScript.

Transfection and transduction experiments

Plasmid transfection experiments

For transfection, HCT116 *WT* cells were reverse transfected for 48 hours with 0.35 μg of FLAG-hRpn13 or empty vector (-) as a negative control (GenScript). Transfection experiments were performed by using Lipofectamine™ 3000 Reagent (Thermo Fisher Scientific) with Opti-MEM® (Life Technologies) reduced serum medium according to the manufacturer's instructions.

Lentivirus transduction experiments

cDNA encoding for ADRM1 (hRpn13) was synthesized (Twist Biosciences) and cloned into pGMC00021 (Addgene) by isothermal assembly[50] to generate the final construct, pMG0784. Plasmid DNA was generated by a maxiprep (Thermo Scientific Fisher) and the cloned plasmid verified by nanopore sequencing (Poochon Scientific). To generate lentivirus, 8 μg of pMG0784, 5.757 μg of psPAX2 (Addgene) and 3.133 μg of pMD.2G (Addgene) were co-transfected using 30 μL of Lipofectamine 2000 into a 15 cm plate of 293T cells. The pMD2.G and psPAX2 plasmids were gifts from Didier Trono. Supernatants from transfected cells were collected at 48 hours and 72 hours, filtered using the Millipore Steriflip 0.45 μm (Millipore) and then concentrated using the LentiX concentrator (Takara) for 3 days as per manufacturer's protocol. The mixture was then centrifuged and re-suspended in ~400 μL of ice cold PBS with 7.2 and 20 μL aliquots made. For the lentiviral transduction of *trRpn13-MM1* or *trRpn13-MM2*, 50,000 cells were transduced with two aliquots of concentrated virus, each of 20 μL, to ensure a high multiplicity of infection for efficient transduction of suspension cells. 48 hours later, cells were spun down at 300 *g* and re-suspended in 200 μL of fresh RPMI media with 10% FBS and 1% Penstrep in a 96 well plate. After approximately one week, cells were collected and transferred to a single well of a 24 well plate. A week later, cells were collected and transferred to a single well of a 6 well plate for an additional week before transferring to a T25 flask.

siRNA knockdown

HCT116 *WT* cells were reverse transfected for 48 hours with 50 nM of commercially available ON-TARGET plus siRNA against hRpn13 (Dharmacon) or with a scrambled non-targeting pool siRNA as a negative control (Dharmacon). Knockdown experiments were performed by using Lipofectamine™ 3000 Reagent (Thermo Fisher Scientific) with Opti-MEM® (Life Technologies) reduced serum medium according to the manufacturer's instructions.

Immunoprecipitation

Cells were trypsinized, flash frozen in liquid nitrogen, and stored at -80°C prior to lysis. Cell pellets were then lysed in native IP buffer (1% Triton X-100, 50 mM Tris-HCl at pH 7.5, 150 mM NaCl) supplemented with protease inhibitor cocktail (Roche), PMSF (100 mM) and ATP nucleotide (100 mM). Protein concentration was determined by a bicinchoninic acid (BCA) protein assay kit (Thermo Fisher Scientific). For hRpn13 or hRpt3 immunoprecipitation, lysates (1 mg total protein) were incubated overnight at 4°C with anti-Rpn13 or anti-Rpt3 antibodies followed by 4-hour incubation at 4°C with Dynabead protein G (Thermo Fisher Scientific). The beads were washed with native IP buffer and the bound proteins resolved and visualized by SDS-PAGE/immunoblotting.

Immunoblotting

Cells were trypsinized, flash frozen in liquid nitrogen, and stored at -80°C prior to lysis in native buffer (1% Triton X-100, 50 mM Tris-HCl at pH 7.5, 150 mM NaCl) supplemented with a protease inhibitor cocktail (Roche), PMSF (100 mM), and PhosSTOP (Roche). Protein concentration was determined by a bicinchoninic acid (BCA) protein assay kit (Thermo Fisher Scientific) after spinning down at 16,000 *g* for 10 minutes at 4°C. 10–20 μg of total protein were loaded on SDS-PAGE (precast Bis-Tris gels, Thermo Fisher Scientific) and transferred onto a 0.45 μm PDVF membrane (Merck Millipore). Immunoblotting of cell lysates was done by incubating overnight with primary antibodies in 5% skim milk or 5% BSA made in Tris-buffered saline with 0.1% Tween-20 (TBST), washing, followed by 1–2 hours of incubation with secondary antibodies at room temperature. After washing, blots were detected by addition of Pierce ECL chemiluminescent reagents (Thermo Fisher Scientific) for HRP-conjugated secondary antibodies.

Immunofluorescence

RPMI 8226 cells grown in 20 mL RPMI 1640 medium in a T75 flask were treated with Annexin V CF488A conjugates and incubated at 37°C in the dark on an orbital shaker for 20 minutes. The cells were spun down at 200 *g* for 10 minutes at 4°C and washed with fresh cell culture media (20 mL) in a T75 flask. The cells were then fixed with 4% formaldehyde by adding 2.4 mL of 37% formaldehyde (Electron Microscopy Science) and incubating on an orbital shaker for 15 minutes at 37°C. Fixed cells were equally distributed between four 50 mL conical tubes, and 45 mL solution of 200 mM Tris pH 8 (for formaldehyde quenching) and 0.1% Triton 100X (for permeabilization) was added to each tube. The cells were then incubated in an orbital shaker for 15 minutes at room temperature and then centrifuged at 200 *g* for 10 minutes at 4°C. The supernatant was carefully aspirated to leave 2-3 mL of solution in which the cell pellets were then resuspended. Suspensions from the 50 mL conical tubes were combined into a 15 mL conical tube. The total number of cells was counted, DAPI nuclear stain (Thermo Fisher Scientific) was added at a final concentration of 5 μg/mL, and the mixture incubated for 30 minutes in an orbital shaker. The cells were centrifuged at 200 *g* for 10 minutes at 4°C and the cell pellet was resuspended in 1X PBS solution to a volume that yields a total number of 1 x 10^6 cells per 1 mL. For each sample, 0.2 mL of this suspension was incubated with phalloidin conjugated to ATTO643 fluorescent dye (ATT0-TEC) or antibodies against β-tubulin TUBB4A (Abcam) that were directly conjugated by a Biotium Mix-n-Stain Kit for CF568 (Biotium), according to the manufacturer's instructions. A 25 mm round cover glass (Thorlabs, CG15XH1) was treated with poly-L-lysine (Sigma) and placed at the bottom of a flat bottom 50 mL tube (Tesc Inc, CT-168000). The tubes were filled with 50 mL of 1X PBS and the 0.2 mL sample

was added with mixing. To attach the cells to the glass, the tubes were centrifuged at 200 *g* for 10 minutes at 4°C and then stored at 4°C until image acquisition. Prior to imaging, the sample on the cover glass was transferred into a Chamlide chamber (Live Cell Instrument, CM-B25-1). Improved image quality was achieved by covering the glass with mounting medium (Biotium). Images were acquired on a Leica DMi8 microscope equipped with a Yokogawa CSU-W1 Spinning Disk Confocal and Andor Zyla 4.2 sCMOS camera controlled by Andor Fusion software, using a 63x NA1.4 oil lens (Leica). Deconvolution was performed with Fusion software. Images were processed in Imaris (BitPlane) and ImageJ software. Immunofluorescence figures are generated as composite images consisting of representative cells from the individual fields of RPMI 8226 *WT*, *trRpn13-MM1* or *trRpn13-MM2* cells.

qPCR

Total mRNA samples from RPMI-8226 *WT*, *trRpn13-MM1*, or *trRpn13-MM2* cells were purified using the RNeasy Plus mini kit (Qiagen), and cDNA was synthesized with the high capacity RNA-to-cDNA kit (Applied Biosystems) according to the manufacturer's instructions. mRNA expression was measured on a qPCR instrument (CFX384; Bio-Rad) using TaqMan probes for UCHL5, hRpn13, MGMT, PADI4, CPNE8, MYO1E, MYH10, ACTN1, TUBB4A, NF-κB1, BTK, GAPDH, β-actin (Applied Biosystems) and 18S ribosomal RNA (Integrated DNA Technology). β-actin, GAPDH and 18S ribosomal RNA were used as internal standards. Fold change in gene expression normalized to the *WT* cells was calculated by using the modified version of efficiency-corrected comparative (Pfaffl equation) method.

Proteasome peptidase assay

RPMI 8226 cells treated for 24 hours with PADI4 specific inhibitor GSK484 (10 μM), carfilzomib (100 nM), or DMSO (vehicle control) were lysed in 0.5% NP-40 lysis buffer. Protein concentration was determined by a bicinchoninic acid (BCA) protein assay kit (Thermo Fisher Scientific) and 10 μg of total protein was used to assay the chymotryptic activity of proteasomes in the presence of AMC-tagged substrate by a commercially available fluorometric proteasome activity kit (Abcam). The manufacturer's instructions were followed but with relative fluorescence determined by using carfilzomib as a negative control.

HDAC8 activity assay

The enzymatic activity of HDAC8 (4 ng/μL) was assayed in the presence of increased concentrations (20, 40, 60 and 80 μM) of purified hRpn13 (1–150) by using the HDAC8 Fluorogenic Assay Kit (BPS Bioscience) according to the manufacturer's instructions. TSA at 100 μM was used as a control of activity inhibition.

Small molecule inhibitor treatment

XL5-VHL2, carfilzomib (Selleck Chemicals LLC), BMS 345541 (Selleck Chemicals LLC), PAD CI-amidine (506282; Sigma) and GSK484 (Abcam or Cayman Chemical Co Inc) were separately dissolved in DMSO and used to treat RPMI 8226 (1 x 10^6 cells) at 40 μM, 100-250 nM or by gradient concentrations for 24 hours. XL5-VHL2 was synthesized as described previously.[14]

Proteome and transcriptome analysis experiments

TMT-MS experiments

Sample preparation. For protein digestion prior to the TMT-MS experiments, the cell pellets were lysed in EasyPrep Lysis buffer (Thermo Fisher Scientific) according to the manufacturer's protocol. Lysates were clarified by centrifugation and protein concentration was quantified by a BCA protein estimation kit (Thermo Fisher Scientific). 20 μg of lysate were reduced, alkylated, and digested by addition of trypsin at a ratio of 1:50 (Promega Corporation) and overnight incubation at 37°C. A pooled sample to mitigate the batch effect was created by mixing equal amounts from each lysate.

Sample labeling. For TMT labeling 100 μg of TMTpro label (Thermo Fisher Scientific) in 100% acetonitrile (ACN) was added to each sample. After incubating the mixture for 1 hour at room temperature with occasional mixing, the reaction was terminated by adding 50 μL of 5% hydroxylamine and 20% formic acid. The peptide samples for each condition were pooled and peptide clean-up was performed using the proprietary peptide clean-up columns from the EasyPEP Mini MS Sample Prep kit (Thermo Fisher Scientific).

Sample fractionation. The TMT peptide mixture was off-line fractionated by high pH reversed-phase chromatography on a Waters Acquity UPLC system with a fluorescence detector (Waters, Milford, MA) using a 150 mm x 3.0 mm Xbridge Peptide BEM™ 2.5 μm C18 column (Waters, MA) operating at 0.35 mL/min. The dried peptides were reconstituted in 100 mL of mobile phase A (3 mM ammonium bicarbonate, pH 8.0) and eluded from the column in mobile phase B (100% ACN, Thermo Fisher Scientific). Before loading the samples, the column was washed with mobile phase A for 10 minutes and the peptides eluded using gradient elution of 0 – 50% phase B (10 – 60 minutes) followed by 50 – 75% phase B (60 – 70 minutes). 80 fractions were collected per minute. The fractions were then consolidated into 24 pools based on the chromatogram intensity, vacuum centrifuged to dryness, and stored at -80°C until analyzed by mass spectrometry.

Mass spectrometry acquisition

The dried peptide fractions were reconstituted in 0.1% trifluoroacetic acid (TFA) and subjected to nanoflow liquid chromatography (Thermo Ultimate™ 3000RSLC nano LC system, Thermo Fisher Scientific) coupled to an Orbitrap Eclipse mass spectrometer (Thermo Fisher Scientific). Peptides were separated with a low pH gradient of 5 – 50% ACN over 120 minutes in the mobile phase with 0.1% formic acid at 300 nL/min flow rate. Full MS1 scans were performed in the Orbitrap at a resolution of 120,000 with an ion accumulation target set at $4e^5$ and max IT set at 50 ms over a mass range of 400 – 1600 m/z. Ions with determined charge states between 2 and 5 were selected for MS2 scans in the ion trap with CID fragmentation (Turbo; NCE 35%; maximum injection time 35 ms; AGC 1 × 10^4).

Data analysis

The acquired MS/MS spectra were searched using the Real Time Search [RTS] Node in the tune file and the human Uniprot database with the Comet search algorithm for TMT (229.163 Da) set as a static modification of lysine and the N-termini of the peptide. Carbamidomethylation of cysteine residues (+57.0214 Da) was set as a static modification, while oxidation of methionine residues (+15.9949 Da) was set up as a dynamic modification. For the selected peptide, an SPS–MS3 scan was performed using up to 10 *b*-type and *y*-type fragment ions as precursors in the Orbitrap at 50,000 resolution with a normalized AGC set at 500 followed by maximum injection time set as ''Auto'' and at a normalized collision energy setting of 65. Reporter ion intensities were adjusted to correct for the impurities according to the manufacturer's specification and the abundances of the proteins were quantified using the summation of the reporter ions for all identified peptides. A two-step normalization procedure was applied on a 6 plex TMT experiment [3 TMT experiments with 2 samples each]. First, the reporter abundances were normalized across all the channels to account for equal peptide loading. Secondly, the intensity from the pooled sample was used to normalize the batch effect from the multiple TMT experiments. Data analysis and visualization were performed in Microsoft Excel and RStudio.

RNA sequencing

Total RNA sample from HCT116 *WT*, *ΔhRpn13*, *trRpn13*, RPMI 8226 *WT*, *trRpn13-MM1* or *trRpn13-MM2* cells were extracted using the RNeasy Plus mini kit (Qiagen) according to the manufacturer's instructions. Illumina sequencing was performed on the HCT116 *WT*, *ΔhRpn13*, and *trRpn13* samples. RNA samples were pooled and sequenced on one hiSeq run using Illumina TruSeq Stranded Total RNA kit (Illumina) and paired end sequencing. Reads of the samples were trimmed for adapters and low-quality bases using Trimmomatic software. Spliced Transcripts Alignment to a Reference (STAR) software was used to align trimmed reads to the reference genome hg19. Gene counts were quantified by STAR using annotations from GenCode Release 19. Transcript abundance was estimated using RSEM then normalized using the voom algorithm and used for differential expression analysis using the 'limma' package (version 3.38.3). All analyses were performed with Python version 2.7.15 and R version 3.5.1.

Gene ontology analysis

We used the Database for Annotation, Visualization and Integrated Discovery (DAVID) to perform gene ontology (GO) analyses. Genes significantly altered with -log(10) (p-value) > 1.3 and $\log_2$ greater than ± 1 were uploaded on DAVID converted to the ''Entrez_Gene_ID'' and analyzed on *Human* species background. We used the default annotation categories with a medium classification stringency for functional annotation clustering analyses, based on which, groups of terms/annotations sharing similar gene members with similar biological meaning are clustered together.

Protein expression and purification

For NMR and biochemical assays, HDAC8, PADI4 and MGMT were expressed and purified from *E. coli* BL21(DE3) cells whereas *E. coli* BL21(DE3) pLysS cells (Invitrogen) were used for hRpn13 (1–150), hRpn13 Pru R16A and hRpn2 (940–953). For HDAC8, MGMT, PADI4, and hRpn2, the cells were transformed and grown at 37°C to an optical density at 600 nm (OD_{600}) of 0.6–0.8 in Luria-Bertani (LB) medium containing antibiotics for selection [50 mg/mL kanamycin (for HDAC8) or 100 mg/mL ampicillin (for MGMT, PADI4 and hRpn2)]. hRpn13 (1–150) was expressed in M9 minimal media with 100 mg/mL ampicillin and ^{15}N ammonium chloride as the sole nitrogen source. Protein expression was induced for ~20 hours at 17°C or 4 hours at 37°C by using 0.4 mM of isopropyl-1-thio-β-D-thiogalactopyranoside (IPTG); 200 μM $ZnCl_2$ was also added at induction for HDAC8. Post-induction, the cells were harvested by centrifugation and resuspended in lysis buffer (50 mM Tris, pH 8.0, 300 mM KCl, 5% glycerol, 1 mM TCEP, 20 μM $ZnCl_2$, 1 mM PSMF and protease inhibitor cocktail for HDAC8; 20 mM Tris, pH 8.1, 400 mM NaCl, 20% glycerol, 2 mM DTT, 5 mM EDTA, 0.5 mg/mL lysozyme and protease inhibitor cocktail for PADI4; 100 mM Tris-HCl, pH 7.34, 300 mM NaCl, 5% glycerol, 2 mM $CaCl_2$, 10 mM $MgCl_2$, 10 mM 2-mercaptoethanol, and protease inhibitor cocktail for MGMT; 20 mM sodium phosphate, pH 6.5, 300 mM NaCl, 10 mM 2-mercaptoethanol, and protease inhibitor cocktail for hRpn13 and hRpn2). Resuspended cells were lysed by sonication and cellular debris removed by centrifugation at 4°C.

For purification of HDAC8, the supernatant was applied to pre-equilibrated Talon Metal Affinity resin (Clontech) and incubated for 2 hours at 4°C for protein binding. The resin was extensively washed with wash buffer A (50 mM Tris, pH 8.0, 300 mM KCl, 5% glycerol, 1 mM TCEP, 1 mM PSMF and protease cocktail) and then wash buffer B (50 mM Tris, pH 8.0, 150 mM KCl, 5% glycerol, 1 mM TCEP). The bound HDAC8 proteins were eluted by incubating the resin with buffer B containing 250 mM imidazole and purity analyzed by SDS-PAGE. Fractions were pooled, concentrated, and then loaded onto a Superdex 200 size exclusion column on an FPLC system (GE Healthcare Life Sciences) pre-equilibrated in buffer B. Protein fractions evaluated by SDS-PAGE, pooled, and concentrated.

For purification of MGMT and PADI4, the supernatant was incubated with glutathione S-sepharose 4B (GE Healthcare Life Sciences) for 3 hours, the resin washed extensively with the lysis buffer, followed by wash buffer (20 mM Tris, pH 8.1, 200 mM NaCl, 10% glycerol, 1 mM DTT, for PADI4) and (100 mM Tris-HCl, pH 7.34, 300 mM NaCl, 5% glycerol for MGMT). PADI4 and MGMT were eluted from the resin by overnight incubation with 50 units per mL of PreScission protease (GE Healthcare Life Sciences).

For purification of hRpn13 (1–150), hRpn13 Pru R16A or hRpn2 (940–953), the supernatant was incubated for 2 hours with Talon Metal Affinity resin (Clontech) or 3 hours with glutathione S-sepharose 4B (GE Healthcare Life Sciences), respectively and the resin washed extensively with buffer C (20 mM sodium phosphate, pH 6.5, 300 mM NaCl, 10 mM βME). hRpn13 (1–150) or hRpn2 (940–953) was eluted from the resin by overnight incubation with 50 units per mL of PreScission protease (GE Healthcare Life Sciences) in buffer D (20 mM sodium phosphate, pH 6.5, 50 mM NaCl, 2 mM DTT). The eluent was subjected to size exclusion chromatography

with a Superdex75 column on an FPLC system equilibrated with buffer D for further purification. For the citrullination experiment, hRpn13 (1–150) and hRpn13 R16A were buffer exchanged and purified by a Superdex75 column on an FPLC system equilibrated with buffer E (10 mM HEPES, pH 7.6, 150 mM NaCl, 1 mM DTT).

Protein concentrations were estimated by using calculated extinction coefficients for each protein and absorbance at $\lambda = 280$ nm.

NMR experiments

The ^{1}H, ^{15}N HSQC experiments involving HDAC8 were performed in NMR buffer 1 (50 mM Tris, pH 7.0, 150 mM KCl, 5% glycerol, 1 mM TCEP, and 10% D_2O); those with MGMT were recorded in NMR buffer 2 (20 mM sodium phosphate, pH 6.5, 50 mM NaCl, 2 mM DTT, and 10% D_2O); and experiments recorded with PADI4 were in NMR buffer 3 (50 mM Tris, pH 7.0, 200 mM NaCl, 5% glycerol, 1 mM DTT, and 10% D_2O). In all cases, comparative spectra were recorded on ^{15}N-labeled hRpn13 (1–150) in identical buffer conditions. Proteins were buffer exchanged into NMR buffer by using Zeba Protein Desalting columns (Thermo Fisher Scientific), with hRpn2 (940–953) pre-mixed with ^{15}N-hRpn13 (1–150) at 2-fold molar excess for 2 hours at 4°C. All NMR experiments were conducted at 25°C on Bruker Advance 600 and 800 MHz spectrometers equipped with cryogenically cooled probes.

Modeling of the HDAC8:hRpn13 Pru complex

HDOCK[33] was used with default parameters to perform molecular docking between hRpn13 Pru and HDAC8. The model with the highest docking score was selected for analysis and display. All figures were generated by using PyMol (PyMOL Molecular Graphics System, http://www.pymol.org).

CITRULLINATION ASSAYS

Citrullination detection by immunoblotting

Citrullination of hRpn13 (1–150) or mutant hRpn13 Pru R16A was assayed by incubating 700 nM purified PADI4 alone or with 2640 nM purified hRpn13 (1–150) or mutant hRpn13 Pru R16A. Similarly, citrullination of the human 26S proteasome (Enzo Life Sciences) was performed by incubating 2100 nM purified PADI4 with 100 nM 26S proteasome in a buffer containing 100 mM HEPES, pH 7.6 and 1 mM DTT in the presence of 10 mM $CaCl_2$ or 5 mM EDTA at 37 °C for 0, 30, 60 and 120 minutes. After incubation, deimination reactions were stopped by adding 1X SDS buffer, followed by boiling at 95 °C for 5 minutes. Citrullination of hRpn13 (1–150) or 26S proteasome was determined by immunoblotting or LC-MS experiments. Immunoblotting was performed by using the Anti-Citrulline (Modified) Detection Kit (Sigma) following the manufacturer's instructions. Following SDS-PAGE, proteins were transferred onto a 0.2 μm PDVF membrane (Merck Millipore), blocked and incubated overnight with primary antibodies.

Citrullination detection by mass spectrometry

A citrullination reaction was also performed for an hRpn13 peptide that spans L11 – N20 by incubating 50 μg of the peptide LVPGSRGASN (synthesized by GenScript) with 500 nM PADI4 in the same buffer as described above for hRpn13 (1–150) with 10 mM $CaCl_2$ or 5 mM EDTA at 37 °C for 120 minutes. Citrullination of hRpn13 (1–150), hRpn13 R16A, and hRpn13 (11–20) was assessed by LC-MS experiments using a 6520 Accurate-Mass Q-TOF LC/MS system equipped with a dual electro-spray source, operated in the positive-ion mode. 10% of acetonitrile was added to each sample before loading onto the instrument. Data acquisition and analyses were performed by Mass Hunter Workstation (version B.06.01).

QUANTIFICATION AND STATISTICAL ANALYSIS

RStudio was used to filter RNA-seq and TMT-MS data excluding genes with *p-value* > 0.05. Spearman Rank correlation plots and statistical analyses were performed by using GraphPad Prism 8. The Mann-Whitney non-parametric test or the Wilcoxon non-parametric test was used for comparison between two groups.